https://doi.org/10.26599/FRICT.2026.9441335

Research Article

Electrically induced superlubricity of electrophoretically deposited graphene-nanoplatelet coatings under aqueous glycerol-lubricated sliding conditions

Parveen Kumar [1,2], Irfan Nadeem [1], Talha Bin Yaqub [1,3], Ardian Morina [2], Mitjan Kalin [1*]

[1] University of Ljubljana, Faculty of Mechanical Engineering, Laboratory for Tribology and Interface Nanotechnology, Aškerčeva cesta 6, Ljubljana 1000, Slovenia

[2] School of Mechanical Engineering, University of Leeds, LS2 9JT, Leeds, UK

[3] CEMMPRE — Centre for Mechanical Engineering Materials and Processes, Department of Mechanical Engineering, University of Coimbra, Rua Luís Reis Santos, 3030-788 Coimbra, Portugal

* Corresponding author: Mitjan Kalin, email id: mitjan.kalin@fs.uni-lj.si

Received: August 23, 2026; Revised: October 21, 2026; Accepted: November 4, 2026

© The Author(s) 2026.

Just Accepted

Abstract

Superlubricity has attracted increasing global interest as an effective strategy for reducing friction-related energy losses in response to rising energy demands. This study demonstrates the feasibility of achieving rapid superlubricity on a steel surface coated with graphene nanoplatelets by controlled electrical stimulation under aqueous glycerol lubrication. The results show that a current of +0.1 A promotes the exfoliation and alignment of the graphene nanoplatelets parallel to the sliding direction. This alignment promotes low-shear interlayer sliding, while detached graphene fragments effectively fill the surface asperities and microcracks, enabling continuous mechanical self-healing. As a result, a

stable early superlubricity regime was established within 145 s, yielding a coefficient of friction (CoF) of ~0.007, and negligible wear. In contrast, a higher current of 3 A triggers excessive electrochemical oxidation and localised thermal effects that overwhelm the defect-healing capability of graphene, leading to insufficient surface passivation, severe wear, accompanied by 9.28-fold increase in CoF (~0.065). This study introduces a novel lubrication strategy for achieving superlubricity under electrified contact conditions and provides fundamental insights into the practical implementation of graphene-based superlubric systems in electrically driven sliding applications.

Keywords: Superlubricity, GNP coatings, Electrophoretic deposition, Electrified sliding, Self-healing mechanism

1. Introductions

The accelerating global demand for energy continues to raise urgent concerns regarding environmental sustainability and climate-change mitigation [1–3]. In this context, frictional losses alone account for nearly 20% of the total global energy consumption, with transportation systems among the major contributors [4]. Electric vehicles (EVs) present a compelling alternative to internal combustion engine (ICE) vehicles, not only because they convert up to ~80% of the electrical energy from the grid into useful motion, compared with only ~20% of the chemical energy in the fuel for ICE vehicles, but also due to their lower greenhouse-gas emissions when powered by renewable energy sources [4–6].

However, despite their environmental and operational advantages, EVs still face several unresolved tribological challenges. Components such as bearings, gears, and electric drivetrains continue to experience significant friction and wear during operation, especially under conditions involving electrical current discharge. These discharges, commonly observed as shaft voltages and bearing currents, arise from the inverter-induced voltage fluctuations, magnetic flux asymmetry, and

Just Accepted

triboelectrical charge build-up, contributing to over 40% of electric motor failures [7–10]. Even relatively small electric motors (e.g., 1.5 kW) have been shown to generate stray currents ranging from 0.2 A to 1.4 A [9,11–13]. Lubrication failures under these conditions can induce instability, vibration, and noise in the bearing system, ultimately leading to severe mechanical degradation and system failure [14–17]. These studies have reported that lubricants with high electrical conductivity and reduced dielectric-breakdown thresholds are more effective in mitigating discharge-induced damage. While traditional lubricants typically have a coefficient of friction (CoF) between 0.01 and 0.1, achieving superlubricity remains a major challenge. Superlubricity, defined as near-zero friction, offers a promising pathway to reduce energy losses, suppress wear, and extend the operating lifetime of engineering components [18].

Recent advances in surface engineering have focused on incorporating two-dimensional (2D) nanomaterials, especially graphene which has demonstrated exceptional potential for reducing friction and wear in electromechanical systems [19–22]. Owing to its low interfacial shear strength, high electrical conductivity, and thermal conductivity, and outstanding mechanical properties, graphene is considered a promising additive for lubricants in electro-tribological applications [20,23]. Its ability to form robust, protective tribofilms under dynamic conditions further strengthens its role [19,24–26]. Furthermore, superlubricity with graphene-family materials has opened a neFw era in solid lubrication [27]. Several studies in non-electrified systems have demonstrated the potential for graphene-based materials to achieve superlubricity**,** particularly when used with aqueous glycerol-based lubricants. For instance, Liu et al. [28] reported a CoF of ~0.004 on SiO_2 substrate by combining glycerol with the pristine graphene coating, while further work [29] achieved CoF values as low as 0.002 and a four-order of magnitude reduction in wear using carboxylated graphene. Ma et al. [30] demonstrated stable superlubricity on steel tribopairs using aqueous glycerol (20 wt.%) within 40 s of testing, and Chen et al. [31] showed that a nanodiamond-glycerol colloidal solution reduced wear and maintained a CoF ≈ 0.006. Nadeem et al. [32] further validated this by using graphene quantum dots in aqueous glycerol

Just Accepted

to achieve super-low friction and enhanced anti-wear performance, with 72% and 53% improvements, respectively. While these studies confirm the potential of graphene in achieving micro- and macro-scale superlubricity in non-electrical systems, its investigation in electrified tribological environments, especially on steel surfaces, remains largely unexplored.

Several studies have reported the role of the graphene under electrical sliding conditions. For example, Berman et al.[33] demonstrated that few-layer graphene maintained a low shear resistance and stable electrical contact during sliding, while Mao et al. [34] and Lang et al. [35] reported significant reductions in friction and wear for graphene-coated surfaces under applied currents. Wang et al. [36] reported a 57% reduction in CoF from ~0.35 to ~0.15 with GO-coated brass. Recently, Wang et al. [37] demonstrated that graphene significantly reduces the friction, wear, and contact resistance at sliding electrical interfaces of copper and brass, across various loads, electrical modes (voltage/current), and testing conditions, highlighting its effectiveness in electrically loaded tribosystems. Furthermore, Hu et al. [38] examined the tribological behaviour of graphene-based nanomaterials as additives in grease under electrical sliding conditions and demonstrated that the graphene exhibits better antifriction and antiwear performance compared to graphene oxide and fluorinated graphene when a ball was connected to negative and disk to the positive terminals of a DC power supply with 0–5 V variations. Notably, Ge et al. [23] achieved macroscopic superlubricity (CoF ~ 0.009) in steel-steel contacts lubricated with polyethylene glycol and graphene oxide solutions under a 0.6 V potential. This finding highlights the potential of superlubricity with graphene-based nanomaterials under electrical sliding conditions.

The present study explores the superlubricity behaviour of electrophoretically deposited (EPD) graphene nanoplatelet (GNP) coatings on 100Cr6 steel substrates under electrical sliding conditions. EPD provides a scalable and eco-friendly method for fabricating uniform, well-adhered coatings on conductive substrates. It offers fine control over the coating's thickness, porosity, and morphology,

Just Accepted

while avoiding the use of toxic solvents or binders [39–41]. The findings of this study provide new insights into the design of graphene-based triboelectrical interfaces, contributing to the development of next-generation surface-engineering solutions aimed at improving the reliability, efficiency, and operating lifetime of components in electromechanical systems.

2. Materials and methods

2.1 Substrate preparation

The tribo-pair consisted of 100Cr6 steel disks (24 mm in diameter) and hardened 100Cr6 steel balls (10 mm in diameter), each with a hardness of 760 $HV_{0.1}$ measured using a micro-Vickers hardness tester (Leitz Miniload, Wetzlar, Germany). The disk samples were mechanically grounded and polished to achieve a mirror-like finish, yielding a surface roughness (R_q) of 10 ± 3 nm. The corresponding ball surfaces exhibited a comparatively higher R_q of 40 ± 5 nm. The 100Cr6 steel disks were used as both the anode and the cathode for deposition purposes. Prior to coating, the samples were thoroughly cleaned with ethanol and isopropanol using an ultrasonic cleaner and were subsequently dried with hot air.

2.2 Electrophoretic deposition of GNPs

GNPs (size < 20 μm) were purchased from the Graphene Supermarket, USA and dispersed in a 70:30 water-ethanol solution at a concentration of 1 mg/mL. The suspension was ultrasonicated for 10 minutes and then magnetically stirred (WiseStir, Germany) for 30 minutes at ambient temperature to achieve a stable and uniform dispersion. The pH of the GNP suspension was measured prior to deposition using a calibrated digital pH meter (Mettler Toledo, Switzerland), and was subsequently maintained in the range 6.8–7.2 to ensure electrochemical stability and consistent deposition behaviour.

Just Accepted

Subsequently, the GNP coatings were applied using EPD process. The schematic of coating deposition procedure is presented in Fig. 1.

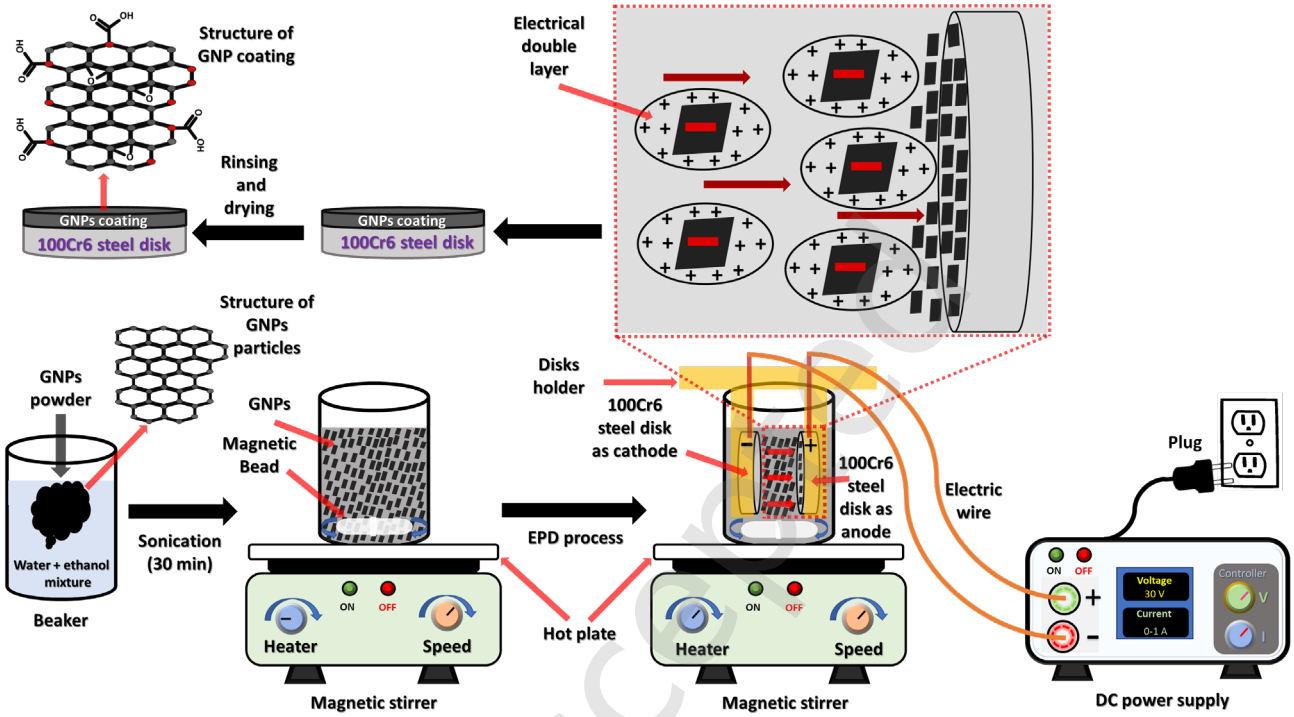


Fig. 1. Schematic of electrophoretic deposition setup used for synthesis of GNP coating.

To maintain the dispersion's stability, the suspension was continuously stirred throughout the deposition process. A stable GNP suspension is essential for the EPD process to ensure the uniform dispersion of individual flakes during deposition. This allows the GNP flakes to migrate independently and deposit without agglomeration. Such stability can facilitates the rearrangement of the graphene sheets during packing, leading to a uniform coating [42]. In a typical configuration, a DC power supply is applied across two parallel electrodes immersed in a solvent (water–ethanol) containing dispersed GNP flakes (see Fig. 1). The thickness of the deposited coating depends on the parameters such as the deposition time, applied voltage, and particle concentration [39,43]. In current study the EPD was carried out at a constant 30 V using a commercial DC power supply for 30 min. Two parallel 100Cr6 steel disk electrodes, serving as the anode and cathode, were positioned opposite each other with a 2-cm inter-electrode distance in the suspension to ensure a uniform electrical field during deposition. The GNP flakes possess a net negative surface charge, primarily due to the residual oxygen-containing

Just Accepted

functional groups or adsorbed ions introduced during the liquid-phase exfoliation or chemical processing. Each GNP flake is surrounded by an electrical double layer (EDL), which provides electrostatic stabilisation and prevents aggregation in the absence of an electrical field [44]. The black flakes with a "–" sign inside each oval denote the negatively charged GNP particles (see Fig. 1), while the surrounding positive charge (+) represent the counter-ions in the diffuse layer. When the electrical field is applied, the negatively charged GNP flakes migrate towards the anode. As the flakes approach this anode, compression of the EDL occurs due to the intensified local electrical field, promoting flake accumulation and adhesion. The gradual accumulation of GNP flakes on the anode results in the formation of a continuous coating. Following deposition, the coated samples were rinsed with deionised water and dried in ambient air at 200°C for 60 minutes using a laboratory furnace to improve the adhesion and enhance the structural integrity of the graphene coatings.

The surface morphology and roughness were characterized using a digital microscope (Nikon LV150) and a 3D optical profilometer in accordance with ISO 4287 standards. The morphology of the GNP coating was further examined using scanning electron microscopy (SEM, JEOL JSM IT100, Japan) and energy-dispersive X-ray spectroscopy (EDS). Raman spectroscopy (XploRA Plus V1.2, HORIBA Scientific, France) was used to evaluate the structural characteristics of both the as-received GNP powder and the deposited coating.

2.3 Friction and wear testing

Friction and wear tests were performed using a reciprocating ball-on-disk tribometer (MFT 5000, Rtec Instruments, USA) under both dry and aqueous glycerol-lubricated sliding conditions. In this configuration, a stationary 100Cr6 steel ball (Ø10 mm) was brought into reciprocating sliding contact with a GNP coated 100Cr6 steel disk of 24 mm in diameter and 10 mm thick. For the lubricated experiments, a bio-renewable glycerol (≥99.5% purity, Sigma-Aldrich, Germany) was mixed with demineralized water (supplied by Krka, Slovenia) in a 3:7 mass ratio and stirred using a WiseStir

Just Accepted

magnetic stirrer (Germany) at room temperature to form a homogeneous aqueous glycerol lubricant. The resulting mixture exhibited a viscosity of 18.2 mPa.s, nearly 98% lower than that of pure glycerol (905.7 mPa.s), making it suitable for achieving extreme boundary-lubrication conditions [45]. The lubricated experiments were conducted using 50 µL droplet of aqueous glycerol. Friction tests were performed under a 5 N normal load for 20 min (generating a maximum Hertzian contact pressure of ~798 MPa and a mean pressure of ~532 MPa), with a sliding speed of 0.1 m/s and a stroke length of 5 mm. The parameters used in this study including the sliding duration were selected on the basis of previous studies [33,37,46,47]. Furthermore, these parameters were chosen to ensure boundary-lubrication conditions.

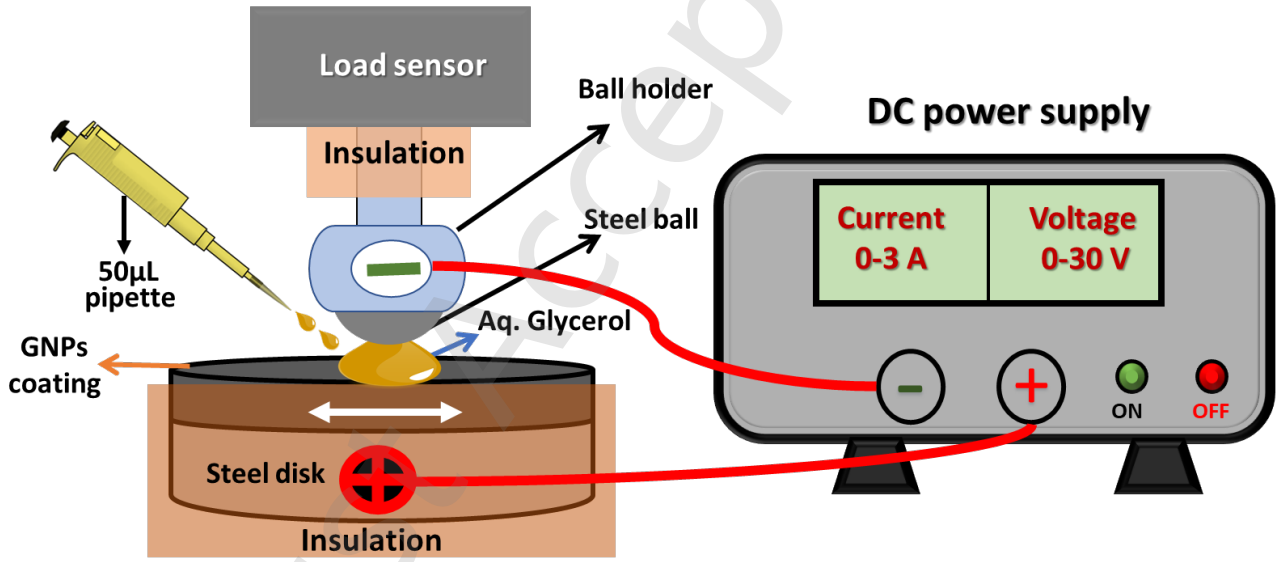


Fig. 2. Schematic of tribometer setup utilised for electrified sliding experiments.

For the electrical testing, the current was varied from 0 to 3 A over a total sliding duration of 20 m using a programmable DC power supply (Good Will Instrument Co., Ltd., Taiwan), while an external voltage of 5 V was also set during sliding. However, the actual voltage is dependent on the contact resistance of the sliding contact interface according to Ohm´s law. The positive terminal of the DC power supply was connected to the disk holder and the negative terminal to the ball holder and electrical insulation was ensured using polyether ether ketone holders for both the disk and the ball to prevent current leakage through the tribometer parts (Fig. 2). Moreover, the tribo-tests were also

Just accepted

conducted by changing the polarity of the current (i.e., −0.1 A), to check the effect on the friction and wear behaviour. All the experiments were conducted at a controlled ambient temperature of 23 ± 2 °C and a relative humidity of 30 ± 5%.

Each test was conducted three times to confirm the results were reproducible. After testing, the wear tracks were carefully cleaned with isopropanol to remove any residual debris before the surface analysis. The wear volume of the steel counterpart ball was calculated using 3D white-light profilometer data with the following equation and the ASTM G133 (2005) standard:

$$V = \left(\frac{\pi h}{6}\right)\left(\frac{3d^2}{4} + h^2\right) \quad (1)$$

Here, V is the wear volume of the steel ball, d is the measured wear-scar diameter, h is the spherical-cap height.

$$h = r - \sqrt{r^2 - \frac{d^2}{4}} \quad (2)$$

r is the original radius of the steel ball, and the specific wear rate of the disk was calculated using the following equation [48]:

$$\text{Specific wear rate} = \frac{\text{wear volume}}{\text{applied load} \times \text{slding distance}} \frac{\text{mm}^3}{\text{Nm}} \quad (3)$$

Just Accepted

2.4 Worn-surface analysis

To investigate the tribo-electrical effects on the tribopair, post-test surface characterization was conducted using a digital microscope (Hirox, HRX-01 & NPS 3D, Japan) and a 3D optical profilometer (ContourGT-K0, Bruker, DE, Germany). These instruments were used to characterize the worn surfaces and quantify the corresponding surface roughness, wear-scar diameter, and wear volume. Raman spectroscopy was conducted within the wear track using a 532 nm excitation laser and a 100× objective lens. To prevent laser-induced damage during the Raman spectroscopy, the laser power was

kept below 5 mW. Additionally, X-ray photoelectron spectroscopy (XPS, PHI-Genesis, Germany) was used to determine the surface chemical composition of the GNP flakes and worn surface after the friction experiment. Measurements were taken at a 90° take-off angle, using the SXI (scanning X-ray imaging) mode for precise localisation within the wear track. A 50 μm X-ray spot size was selected to ensure the signal was collected exclusively from the worn region. The survey spectra were acquired using a 224.0 eV pass energy and a step size of 0.8 eV. Afterwards, HR C 1s, O 1s, and Fe $2p_{3/2}$ were acquired using a 27 eV pass energy and 0.1 eV step size. The element concentrations on the surface were determined using relative sensitivity factors determined in the manufacture's handbook [49]. Together, these multi-scale structural and compositional analysis enabled a comprehensive evaluation of the GNP coating's integrity, chemical transformations, wear mechanism, and structural evolution under coupled electro-mechanical loading.

3. Results

3.1 Characterisation of GNP coating

Fig. 3a-b presents an optical micrograph and an SEM surface-topography image of the GNP coating, showing an almost uniform graphene-nanoplatelet coating across the steel substrate. This surface analysis indicates effective surface coverage without any obvious agglomeration or defects. Moreover, an EDS maps analysis (Fig. 3b) was conducted to identify the elements present on the GNP coated steel surface. The EDS mapping (Fig. 3b) shows that the coating is mainly carbon-rich, with the carbon and oxygen being ~88.31 at. % and ~6.65 at. %, respectively. Such a large amount of carbon indicates that the surface is largely covered with GNP particles having limited surface oxidation. The presence of Fe (~3.84 at. %) and Cr (~1.2 at. %) in the EDS spectra arises due to the relatively large electron interaction volume relative to the ~1.25-μm thick graphene coating, allowing X-rays generated in the 100Cr6 steel substrate to escape through the carbon layer. The coating thickness (~1.25 μm) was measured using 3D optical profilometry as shown in Fig. 3c. A similar approach to measure the coating-thickness was reported by Wang et al. [37]. The uniform morphology and relatively consistent

Just Accepted

coating thickness suggest effective deposition and uniform substrate coverage, providing a stable base for tribological testing.

The Raman spectroscopy was performed on the coated surface and the resulted spectra is shown in Fig. 3d. The Raman spectrum of the GNP powder exhibits characteristic D, G and 2D bands at 1344 cm^{-1}, 1577 cm^{-1} and 2711 cm^{-1}, respectively, with an I_D/I_G ratio of ~0.10, confirming a relatively low defect density and a well-preserved sp^2 carbon network. Similarly, the as-deposited GNP coating exhibited a relatively low D-band at ~1351 cm^{-1}, a sharp G band centred at ~1587 cm^{-1}, and a symmetric 2D-band at ~2718 cm^{-1}. The D-band is associated with defect-activated/disordered carbon, whereas the G-band corresponds to the in-plane vibration of sp^2-bonded carbon atoms and its presence reflects the crystallinity of the graphitic structure [50,51]. The as-deposited GNP coating shows a slight increase in disorder (I_D/I_G ratio ~0.17), compared to the GNP powder, suggesting that the as-deposited coating has a low defect density, while the presence of a higher-order and broadened 2D-band feature indicates the multilayer structure of the graphene coating [32,52,53]. In addition, the I_{2D}/I_G ratio of 0.28 for the as-deposited coating further suggests a multilayer morphology, consistent with the platelet structure of the GNPs [32].

The XPS analysis was conducted to verify the functional groups and to determine the chemical composition of the coating (see Fig. 3e). The high-resolution C 1s spectrum of the graphene coating was deconvoluted into five components. The dominant peak at 284.5 eV corresponds to C–C/C=C (54.08%), confirming the preservation of the graphitic structure [54]. Additional components at binding energies of 285.6 eV (C–O), 287.0 eV (C=O), and 288.3 eV (O–C=O) are attributed to the oxygen-containing functional groups, which may have been introduced during deposition of the graphene coating [50]. The final component at 290.6 eV corresponds to π-π* transitions in the graphitic carbon. The oxygen-containing functional groups were present in relatively small amounts and were expected to play a supportive role by improving the interfacial adhesion between the graphene coating

Just Accepted

and the steel substrate. The XPS findings are fully consistent with the Raman results and confirm the presence of a structurally ordered graphene coating with limited oxidation. This balanced surface chemistry is characterised by a graphitic carbon backbone complemented by a controlled level of oxygen functionalities, which provides a favourable combination of interfacial stability and lubricating efficiency.

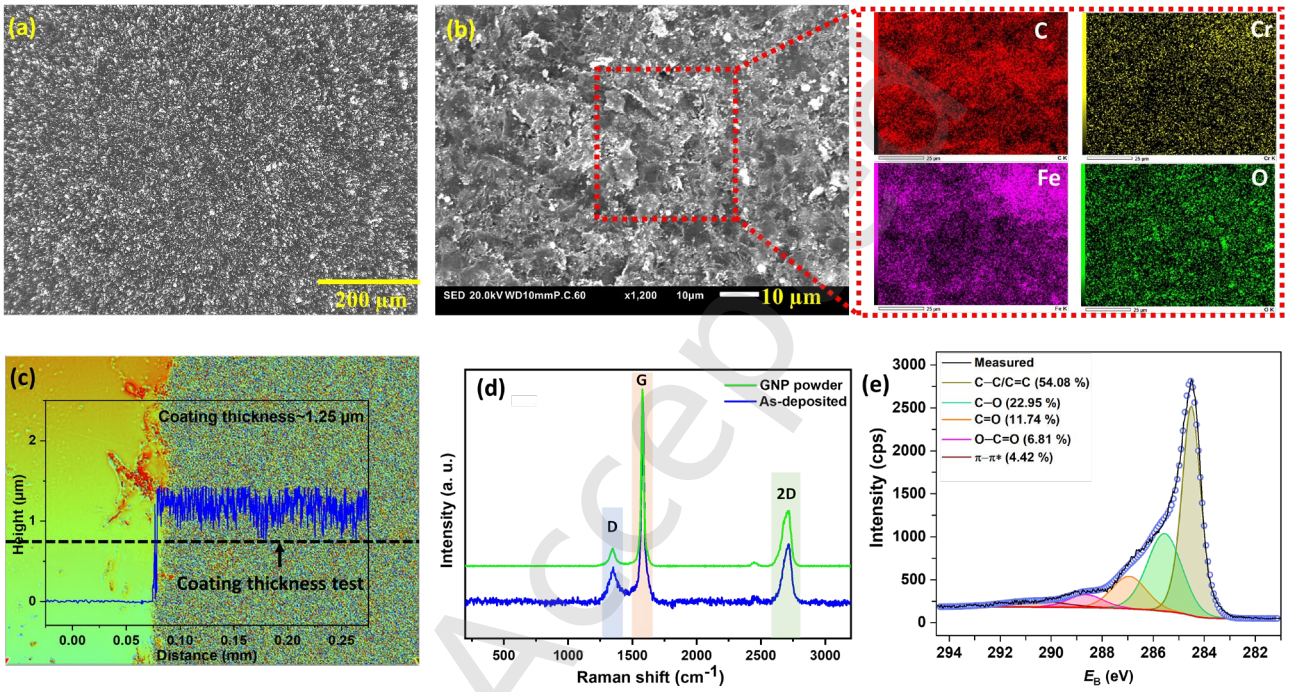


Fig. 3. Characterisation of GNP coating (a) Optical microscopy image, (b) SEM morphology micrograph and EDS elemental mapping of the selected area, (c) Coating thickness measurement using 3D profilometer, (d) Raman spectra of GNP powder and as-deposited coating, and (e) XPS analysis of the as-deposited coating.

Just Accepted

3.2 Friction behaviour

The tribological performance results under dry and lubricated conditions with and without electrical stimulation is presented in Fig. 4. The baseline test on the uncoated steel substrate under dry sliding conditions without an electrical current exhibited a clear running-in phase, with the steady-state CoF stabilizing at ~0.57 after ~200 s. In contrast, the GNP coated steel showed a considerable reduction in CoF (~0.083), maintaining stable friction throughout the test with very short running-in phase (Fig. 4a). Further, the influence of electrical stimulation on the tribological performance of the GNP coating

was systematically examined under aqueous glycerol lubrication, with applied currents ranging from 0 to 3 A and a voltage of 5 V; however, the actual voltage across the sliding contact interface was governed by the contact resistance, in accordance with Ohm's law. As a preliminary step, tests were performed under low current polarity (±0.1 A) to assess the coating's stability under dry sliding conditions (Fig. 4b).

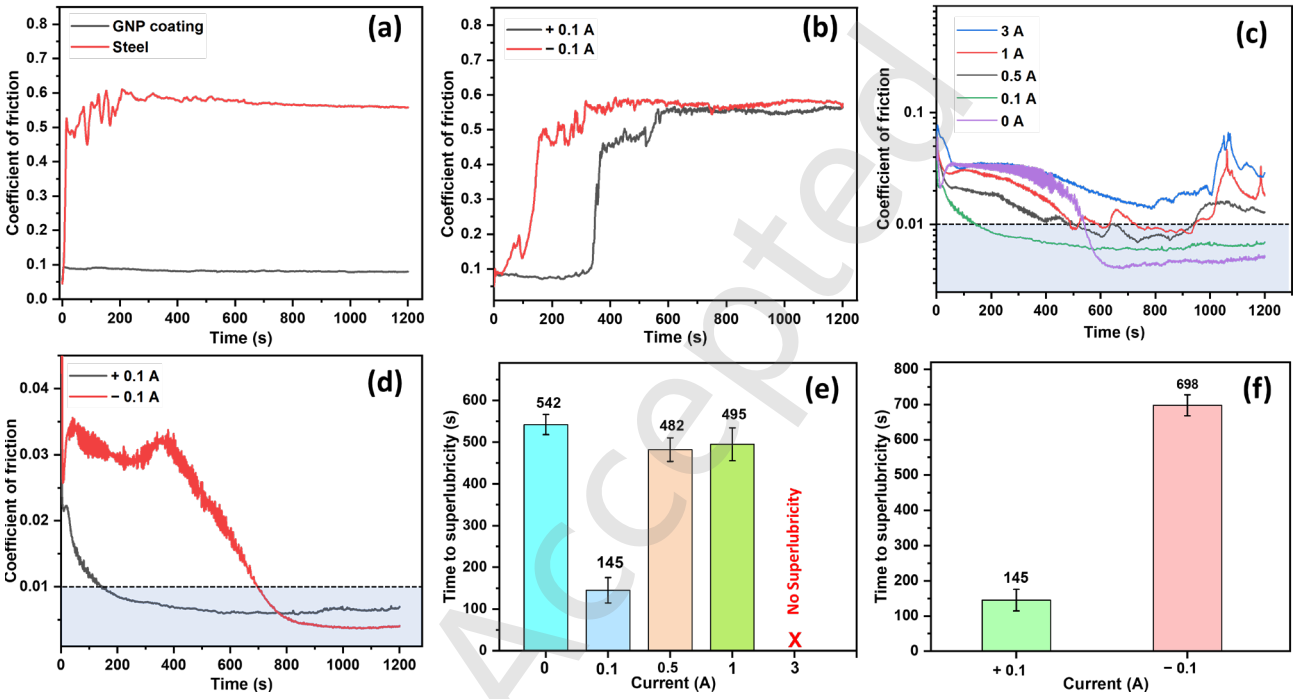


Fig. 4. Coefficient of friction versus time for (a) steel and GNP coating, (b) GNP coating with electrical current of +0.1 and −0.1 A under dry sliding condition, (c) GNP coating with electrical current of 0 to 3 A, and (d) GNP coating with electrical current of +0.1 and −0.1 A under aqueous glycerol-lubricated sliding condition. (e) Time to reach superlubricity region with electrical current of 0 to 3 A, and (f) Time to reach superlubricity region with electrical current of +0.1 and −0.1 A under aqueous glycerol-lubricated sliding condition.

The coating failed after ~100 s and ~370 s with –0.1 A and +0.1 A, respectively, and the corresponding average CoF values were ~0.51 and ~0.40, respectively, indicating poor electrochemical stability under dry current-carrying sliding conditions. In case of the lubricated tests without an applied electrical current (0 A), the GNP coated steel exhibited enhanced tribological performance as compared to dry sliding. The CoF gradually decreased from ~0.041 to ~0.005 and reached a stable superlubricity state after a running-in time of ~542 s (Fig. 4c). However, the long running-in time required to attain superlubricity may raise concerns about potential wear accumulation on the tribo-pairs during the early

Just Accepted

stages of sliding. Based on the results observed under dry sliding conditions with positive and negative current polarity, all the subsequent tests were conducted under positive current polarity using aqueous glycerol-lubricated sliding conditions.

At +0.1 A the GNP coating achieved a superlubricity regime (CoF ~0.007) within just ~45 s (Fig. 4e) compared to 0 A (~542 s) and remained in a stable superlubricity state throughout the test. An increase in the current to 0.5 A resulted in a stable ultra-low-friction regime, with the CoF maintained at ~0.014. However, the superlubricity state was achieved after ~482 s and remained upto ~950 s (Fig. 4c and e). Under 1 A, the increase in current caused only a slight rise in the average CoF (~0.017-0.027). The CoF entered the superlubricity state after ~495 s and remained in that sate up to ~ 960 s; however, no superlubricity state was achieved with 3 A (Fig. 4c and e). The CoF behaviour exhibited more pronounced frictional fluctuations towards the end of the tests with both 1 and 3 A, indicating increasing instability and degradation of the graphene tribofilm under higher electrical currents. Correspondingly, the CoF increased to ~0.05 and ~0.065 towards the end, respectively (Fig. 4c). Interestingly, the superlubricity was also achieved when the current polarity was switched from positive to negative (i.e., −0.1 A), although after a prolonged sliding duration (~698 s), and remained in that regime, similar to the 0 A condition, but with a delayed onset compared to +0.1 A (Fig. 4d and f). This behaviour demonstrates a similar trend to that observed under dry electrical stimulation with reversed polarity (i.e., running-in time increased).

These findings highlight the critical influence of the magnitude of current and polarity on the frictional performance of the GNP coating. The rapid onset of superlubricity under +0.1 A and the delayed transition under −0.1 A suggest that the direction of the charge flow affects the tribolayer formation and stability. The stable low-friction regime at moderate positive currents, along with increased fluctuations at higher currents, suggests that excessive electrical loading may lead to tribolayer degradation. Overall, electrical stimulation emerges as a critical factor in modulating the lubricating

Just Accepted

behaviour at the sliding interface of GNP coatings under aqueous glycerol-lubricated sliding conditions, and is discussed in a later section.

3.3 Wear behaviour

The GNP coating improves the wear resistance of the tribological pair under dry sliding conditions. Fig. 5 presents an optical micrograph of the counter steel ball showing the wear-scar diameter. Compared to the uncoated steel surface, the presence of GNP leads to a noticeable reduction in the wear diameter on the counterface steel ball, with the wear-scar diameter decreased by ~88.3% from ~1300.5 μm to ~152.78 μm (see Fig, 5a-b), corresponding to final contact pressures of ~3.76 MPa and ~272.74 MPa, respectively. The post-test final contact pressure was estimated by dividing the applied normal load to the measured wear-scar area after each test [55,56]. This highlights the effectiveness of the GNP coating in mitigating the surface damage, enhancing the load-bearing capacity, and prolonging the lifetime of component. Under the application of electrical current under dry sliding, the wear-scar diameter was ~1102 μm at +0.1 A with a corresponding final contact pressure of ~5.24 MPa (Fig. 5c) and the surface was relatively smoother. Overall, the wear-scar diameter remained smaller than that of the uncoated steel tested without current. The edge of the boundary contact zone exhibited some residual dark patches, likely a compacted carbon-rich film transferred from the GNP coated disk. In contrast, negative current polarity (−0.1 A) caused a further increase in the wear-scar diameter to ~1233.5 μm, slightly higher (~12%) than that observed at +0.1 A and thus, the final contact pressure also reduced (i.e., ~4.18 MPa) as shown in Fig. 5d, and the surface exhibited more pronounced grooves and brighter metallic regions.

The 3D surface topography and wear profiles of the ball scars are shown in Figs. 6, 8 and 9. The topographic data were corrected for the specimen tilt and spherical curvature using the unworn regions surrounding the scar as the reference surface. Cross-sectional profiles were then extracted across the wear-scars, and the maximum wear-scar depth was determined as the vertical distance between the corrected reference surface, and the deepest point within each scar. Under dry sliding without current,

Just Accepted

the steel-steel contact exhibited surface roughness (S_q) of ~179 nm (Fig. 6a-i), and a wear depth of ~36.48 µm (6a-ii), which indicates dominant adhesive and oxidative wear. However, the GNP coating significantly reduced the surface roughness (i.e., ~68.62 nm, (Fig. 6b-i)), and suppressed ball wear to a negligible depth of ~0.33 µm (Fig. 6b-ii)). This implies that graphene detached and form a continuous carbon-rich tribofilm at the interface, which carries load and prevents severe abrasion [57,58]. Under the +0.1 A conditions, the surface roughness and wear-scar depth of the ball increased to ~157 nm (see Fig. 6c-i), and ~25.70 µm (Fig. 6c-ii), respectively. However, the reverse current polarity (−0.1 A) further increased the roughness (i.e., ~240 nm) and wear-scar depth to ~37.64 µm (see Fig. 6d(i-ii)), highlighting the degradation of the coating under dry electrified sliding, resulting in higher friction (see Fig. 4b) and wear (see Fig. 7b and 8b), compared to the +0.1 A sliding condition.

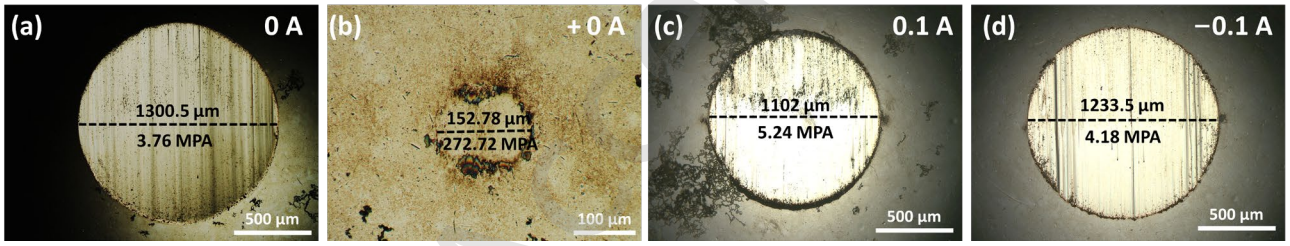


Fig. 5. Optical micrograph of counter steel ball wear track sliding with (a) steel, (b) GNP coating without electrical current. Sliding against GNP coating with electrical current of (c) + 0 .1 A, and (d) −0.1 A under dry sliding condition.

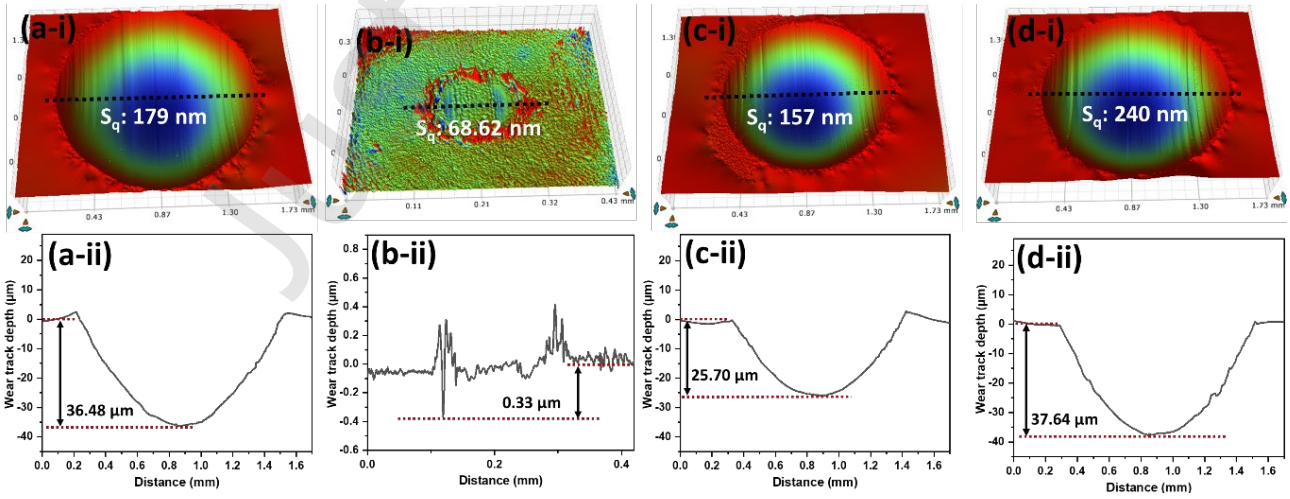


Fig. 6. 3D images and corresponding profiles of counter steel ball wear-scar after dry sliding without electric current (a-i) after sliding with bare steel disk, (a-ii) corresponding wear scar depth profile, (b-i) after sliding with GNP coated steel disk, (b-ii) corresponding wear scar depth profile. Sliding against GNP coating under dry electrified sliding conditions of (c-i) +0.1 A, (c-ii) corresponding wear scar depth profile and (d-i) −0.1 A, (d-ii) corresponding wear scar depth profile.

Just Accepted

Furthermore, the optical micrographs show the evolution of the wear-scar on a steel ball sliding against a GNP coated disk under different applied electrical currents in an aqueous glycerol-lubricated environment (see Fig. 7). At 0 A (Fig. 7a) the wear-scar diameter was ~264.5 µm, with a final contact pressure of ~91 MPa. Under +0.1 A (Fig. 7b), the wear-scar diameter reduced to ~240 µm, indicating an ~9.3% reduction compared with the 0 A condition, while the contact pressure increased by ~21.5% (~110.52 MPa). Notably, the final contact pressure achieved in the present study was nearly three times higher than that reported by Ge et al. [23] (i.e. 36.5 MPa at 0.6 V), highlighting the high load-bearing capability achieved under the present electro-lubricated configuration. The surface appears smooth and uniform with shallow tracks, which suggests that a slight positive current enhances the protective effect of the GNP coating, likely by improving the alignment and adhesion of the nanoparticles on the surface.

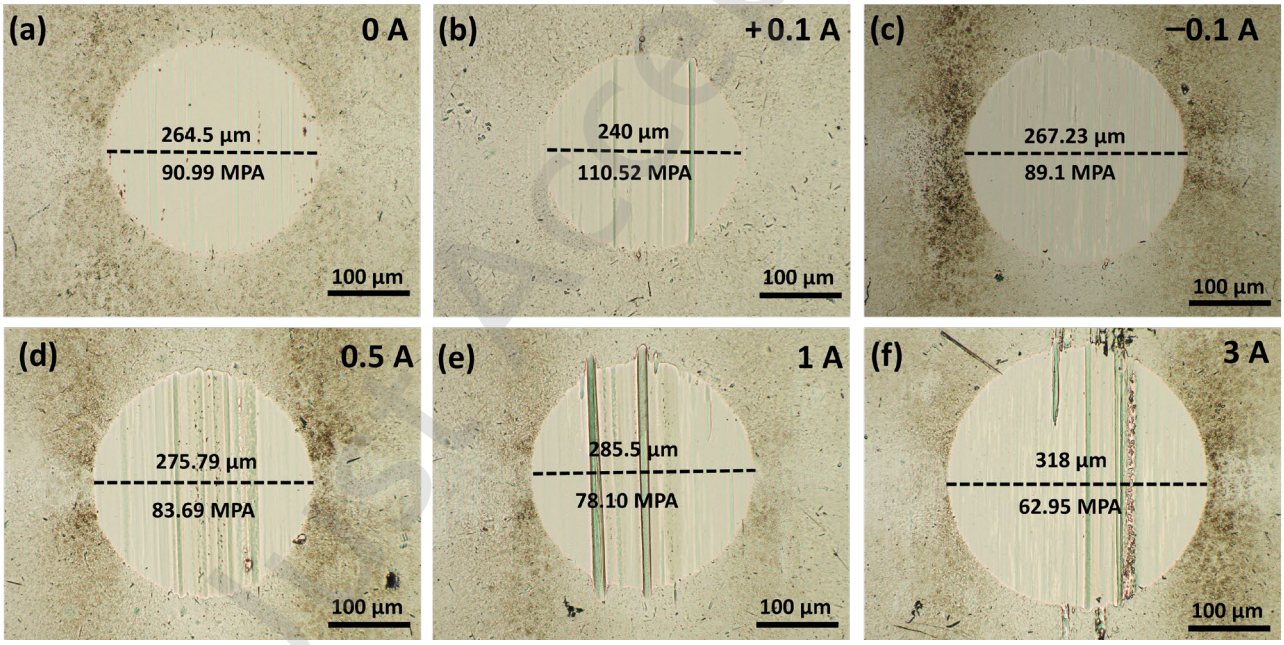


Fig. 7. Optical micrograph of counter steel ball wear track sliding against GNP coated disk under electrical currents in presence of aqueous glycerol-lubricated sliding condition at (a) 0 A, (b) +0.1 A (c) −0.1 A, (d) 0 .5 A, (e) 1 A, and (f) 3 A.

Interestingly, when the current polarity was reversed (i.e., −0.1 A, see Fig. 7c), the wear-scar diameter increased to ~267.23 µm, corresponding to increase of ~1.03% and ~11.35% compared with 0 A and +0.1 A, respectively, while the final contact pressure slightly decreased to ~89.1 MPa (~2.1% lower than at 0 A). This suggests that the negative polarity slightly reduces the coatings effectiveness, likely

due to a minor displacement of the GNP, but does not cause severe damage compared to higher positive currents. As the positive current increased to 0.5 A and 1 A (Fig. 7d and 7e), the wear-scar diameters increased to ~275.79 µm and ~285.5 µm, respectively, corresponding to increases of ~4.27% and ~7.94% compared with the 0 A condition. The corresponding final contact pressures decreased to ~83.69 and ~78.10 MPa, representing reductions of ~8.0% and ~14.2%, respectively. This trend indicates that moderate positive currents begin to slightly deteriorate the lubricating effect, possibly due to an increased electrochemical disruption of the GNP layer. Further, at the higher current of 3 A (Fig. 7f), the wear-scar diameter increased to ~318 µm, representing a ~20.2% increase compared with the 0 A condition, while the contact pressure further decreased to ~62.95 MPa, corresponding to a ~30.8% reduction relative to 0 A. This considerable increase in scar diameter suggests that a higher current deteriorates the GNP coating and accelerate the abrasive wear during sliding, reducing the overall protective effect.

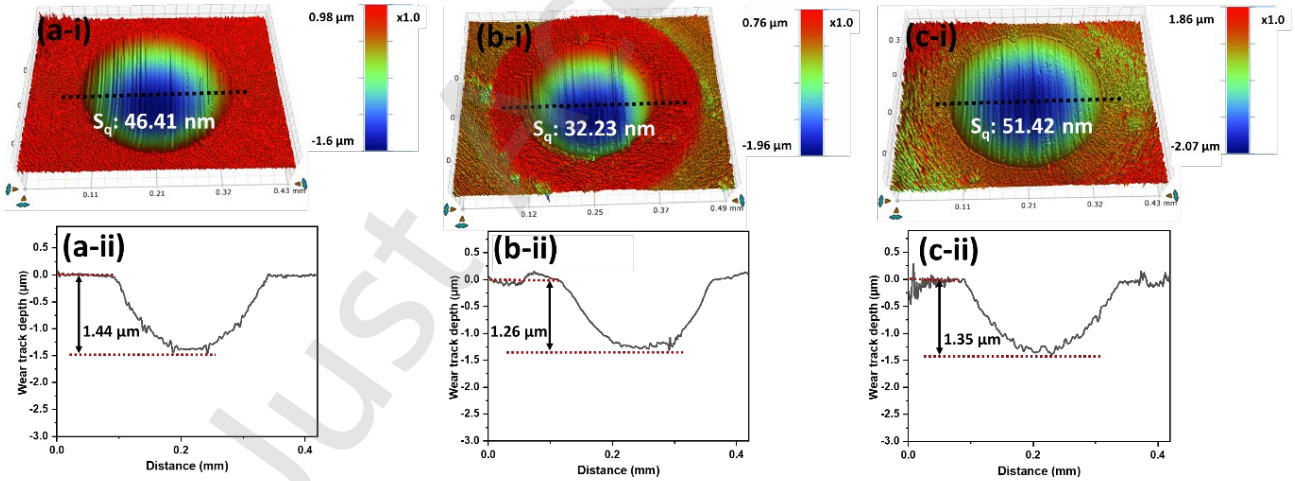


Fig. 8. 3D images and corresponding profiles of counter steel ball wear-scar after lubricated sliding against coated disk with electrical current of (a-i) 0 A (a-ii) corresponding wear scar depth profile, (b-i) +0.1 A, (b-ii) corresponding wear scar depth profile and, (c-i) −0.1 A, (c-ii) corresponding wear scar depth profile.

3D interferometry shows a low surface roughness (~46.41 nm, see Fig. 8(a-i)), and the wear depth (~1.44 µm, see Fig. 8(a-ii)) compared to dry sliding. Importantly, applying a positive current (+0.1 A) further enhanced this lubricated state, while the surface roughness and ball wear depth were reduced by ~30.5% (32.23 nm) and ~12.5% (1.26 µm), respectively (see Fig. 8b(i-ii))), compared to the 0-A

Just Accepted

lubricated condition. However, with reverse polarity (−0.1 A), the roughness, and wear depth were increased to 51.42 nm, and 1.35 µm, respectively (see Fig. 8c (i-ii)) compared to the +0.1 A sliding conditions. Moreover, Fig. 9a-c shows the surface roughness of the steel ball increased to 72.27 nm, 95.08 nm, and 144 nm with increasing the applied currents i.e., 0.5 A, 1 A, and 3 A, while the wear depth also increased to 1.49 µm, 2.28 µm, and 2.68 µm, respectively (see Fig. 9a-c), compared to 0 A sliding. These results suggest that a modest electrical stimulation plays a pivotal role in suppressing wear, likely through modulation of the interfacial charge dynamics and tribolayer formation.

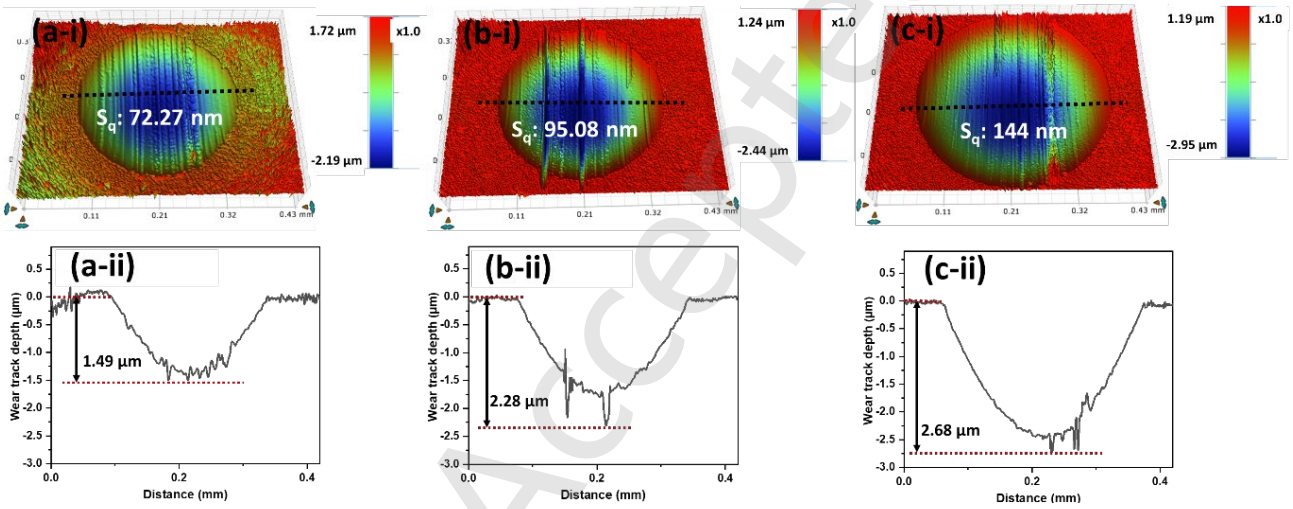


Fig. 9. 3D images and corresponding profiles of counter steel ball wear-scar under lubricated sliding against coated disk with electrical current of (a-i) 0.5 A, (a-ii) corresponding wear scar depth profile, (b-i) 1 A, (b-ii) corresponding wear scar depth profile and, (c-i) 3 A, (c-ii) corresponding wear scar depth profile.

Furthermore, based on the wear-scar diameter, the wear volumes of the counter steel balls were calculated, which depends on the contact material (coated or uncoated), current polarity, and lubrication environment, as shown in Fig. 10. Under dry sliding (Fig. 10a), the GNP coating provided a strong protective effect compared to an uncoated steel. The wear volume decreased drastically from ~2.80×10^{-2} mm^3 for the uncoated steel to ~5.22×10^{-6} mm^3 for the GNP coated steel, corresponding to an almost complete suppression of material loss (~99.98% reduction). As already discussed, the polarity of the applied current influenced the tribological performance, even at very low currents. The positive current polarity (+0.1 A) reduced the wear volume to ~1.5×10^{-2} mm^3, while under −0.1 A, increased to ~2.2×10^{-2} mm^3 (Fig. 10b). This represents an increase in wear volume of about ~46.7%

Just Accepted

when switching from positive to negative polarity, indicating that the direction of electron flow affects the stability of the tribolayer under dry sliding conditions.

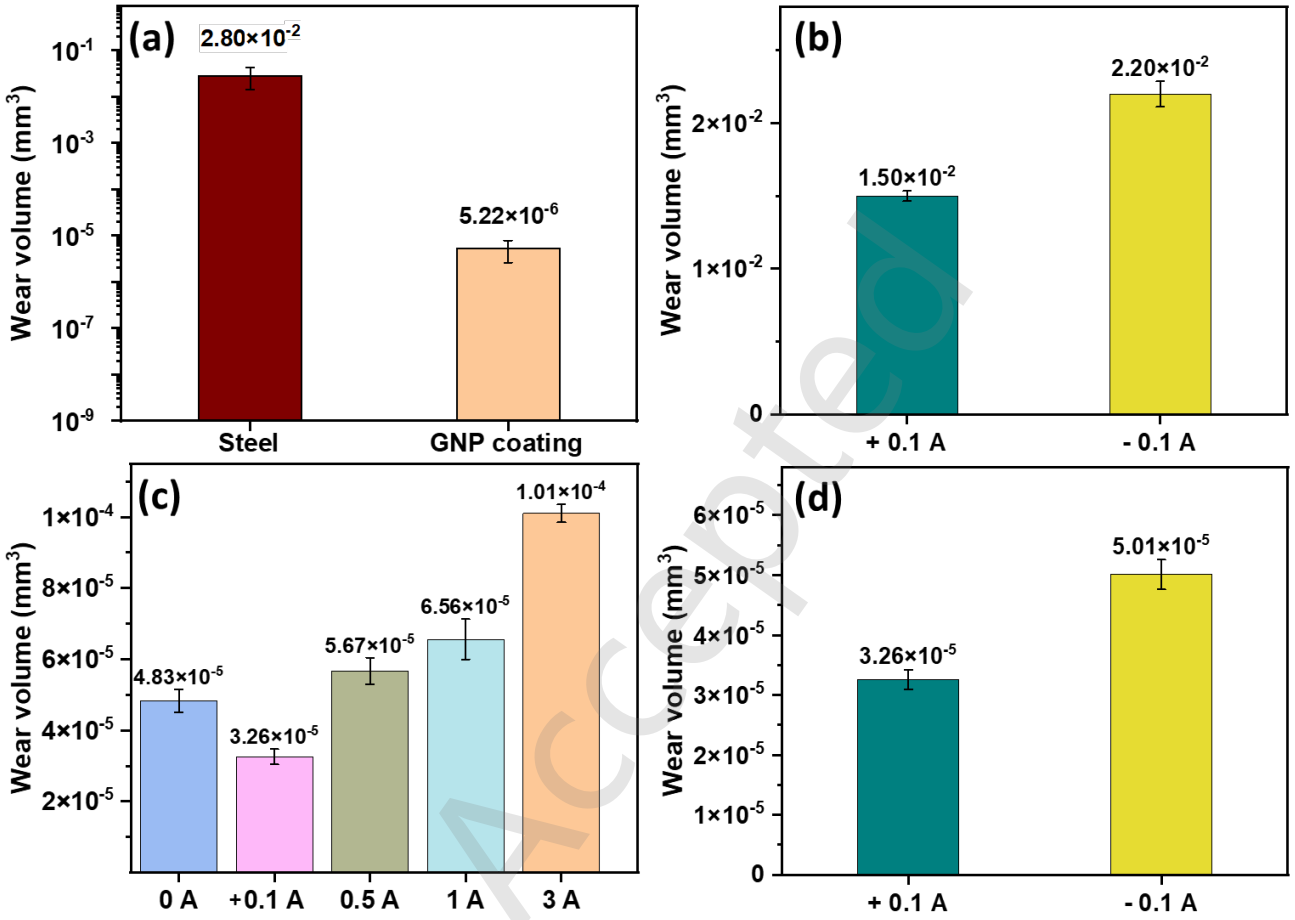


Fig. 10. Wear volume of counter steel ball sliding against (a) uncoated steel and GNP coated steel, and (b) GNP coated steel under applied electrical current of +0.1 and −0.1 A under dry sliding condition, and against (c) GNP coated steel with electrical current of 0 to 3 A, and (d) GNP coated steel with electrical current of +0.1 and −0.1 A under lubricated sliding.

In the aqueous glycerol-lubricated condition (Fig. 10c-d), the influence of current was even more pronounced. At 0 A, the wear volume was ~4.83 × 10^{-5} mm^3 (Fig. 10c). Notably, applying a positive current (+0.1 A) led to the most favourable anti-wear response, as evidenced by the reduction in wear volume (Fig. 10c) by ~32.5% (3.26 × 10^{-5} mm^3) compared to 0 A. However, as the current increased further, the beneficial effect diminished. At 0.5 A and 1 A, the wear volume increased by ~17.4% (5.67 × 10^{-5} mm^3) and ~35.8% (6.56 × 10^{-5} mm^3), respectively, compared with that observed at 0 A. At the highest current of 3 A, the wear volume increased to ~1.01 × 10^{-4} mm^3, more than double the 0 A value (~109% increase). This trend suggests that a mild current helps to stabilize the GNP film in aqueous

Just Accepted

glycerol, whereas a high current promotes tribolayer breakdown, thereby increasing the wear [36]. Current polarity again shows a strong influence in the lubricated tests. The wear volume at −0.1 A (Fig. 10d) increased to ~5.01 × 10^{-5} mm^3, which was ~53.7% and ~3.7% higher than +0.1 A and 0 A, respectively. This difference indicates that a negative current destabilizes the interface more severely, possibly due to electrochemical effects at the contact. Overall, the results suggest that the GNP coating protects the steel ball and positive currents further enhance the wear performance, whereas negative polarity and higher currents (0.5-3 A) increase the wear by disturbing the protective tribolayer.

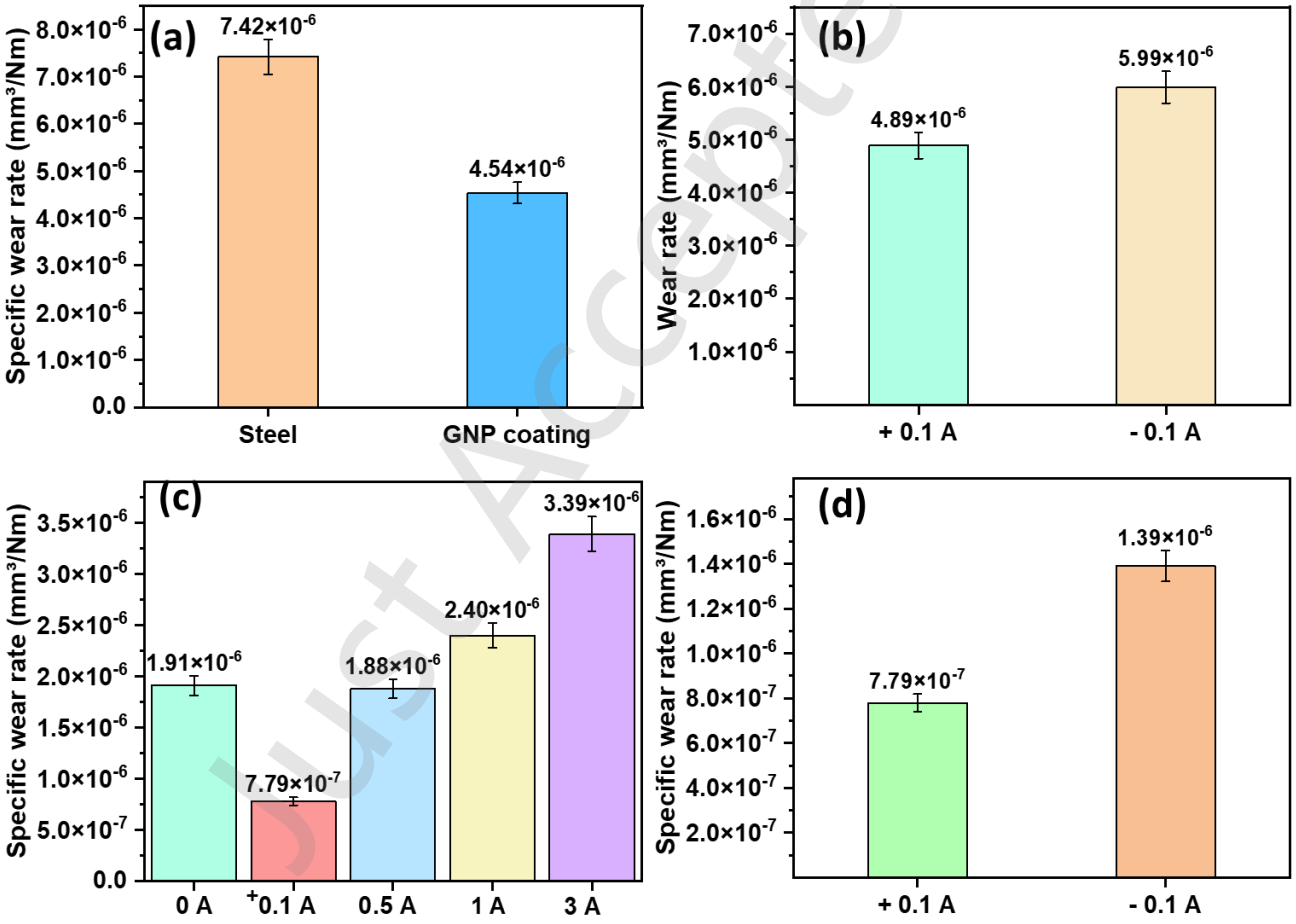


Fig. 11. Specific wear rate of GNP coated disk sliding against (a) uncoated steel and GNP coated steel, (b) GNP coated steel with electrical current of +0.1 and −0.1 A under dry sliding condition, and against (c) GNP coated steel with electrical current of 0 to 3 A, and (d) GNP coated steel with electric current of +0.1 and −0.1 A under aqueous glycerol-lubricated sliding.

The specific wear rate of the uncoated and GNP coated steel disk was also calculated. Fig. 11 shows clear differences in the wear-rate behaviour of the steel and the GNP coated disk under dry and

Just Accepted

lubricated with different electrical currents sliding conditions. Under dry conditions (Fig. 11a), the uncoated steel disk exhibits a wear rate of ~7.42 × 10^{-6} mm^3/Nm, while the GNP coating reduces this to about ~4.54 × 10^{-6} mm^3/N·m, which corresponds to a reduction of nearly ~38.8% in wear rate compared to uncoated steel. Under dry sliding, the wear rate response was strongly influenced by the polarity of the applied current. At +0.1 A, the GNP coated disk exhibited a wear rate of about 4.89 × 10^{-6} mm^3/Nm, whereas applying −0.1 A (negative polarity) increased it to ~5.99 × 10^{-6} mm^3/Nm, corresponding to an ~22.5 % increase in wear after switching from positive to negative polarity (see Fig. 11b).

In the aqueous glycerol-lubricated condition (Fig. 11c), the effect of the current magnitude became more pronounced. At 0 A, the wear rate was about ~1.91 × 10^{-6} mm^3/Nm. Applying a positive current (+0.1 A) lowered the wear rate to ~7.79 × 10^{-7} mm^3/Nm, which represents a reduction of nearly ~59% compared with 0 A. At 0.5 A, the wear rate was ~1.88 × 10^{-6} mm^3/Nm, approximately ~1.6% lower than that at 0 A. Further increasing the current to 1 A raised the wear rate to ~2.4 × 10^{-6} mm^3/N·m, an increase of about ~26 %, and the highest current of 3 A increased it to nearly ~3.39 × 10^{-6} mm^3/N·m, corresponding to an increase of about ~78 % compared with the 0 A current. Moreover, the current polarity under lubrication also has a strong impact. At −0.1 A (negative polarity), the wear rate increased to ~1.39 × 10^{-6} mm^3/Nm (Fig. 11d), which corresponds to an increase of ~78% compared to +0.1 A (positive polarity), showing that negative polarity was also not favourable under aqueous glycerol lubrication. Overall, these results show that the GNP coating reduces the wear compared to bare steel, positive current polarity improves performance, especially in lubricated contacts, whereas negative polarity and higher current intensities (with positive polarity i.e., 1–3 A) leads to higher wear by disturbing the protective tribolayer.

3.4 Raman spectroscopy of worn surfaces

To gain an insight into the structural transformations of the GNP coating during sliding and to clarify the mechanisms driving its frictional and wear behaviour under dry and lubricated conditions with

Just Accepted

electrical stimulation. Raman spectroscopy was performed on most of the GNP particles present within the wear tracks that are shown in **Fig. S1,** to evaluate defect formation in the graphene structure, and the corresponding Raman spectra are presented in Fig. 12.

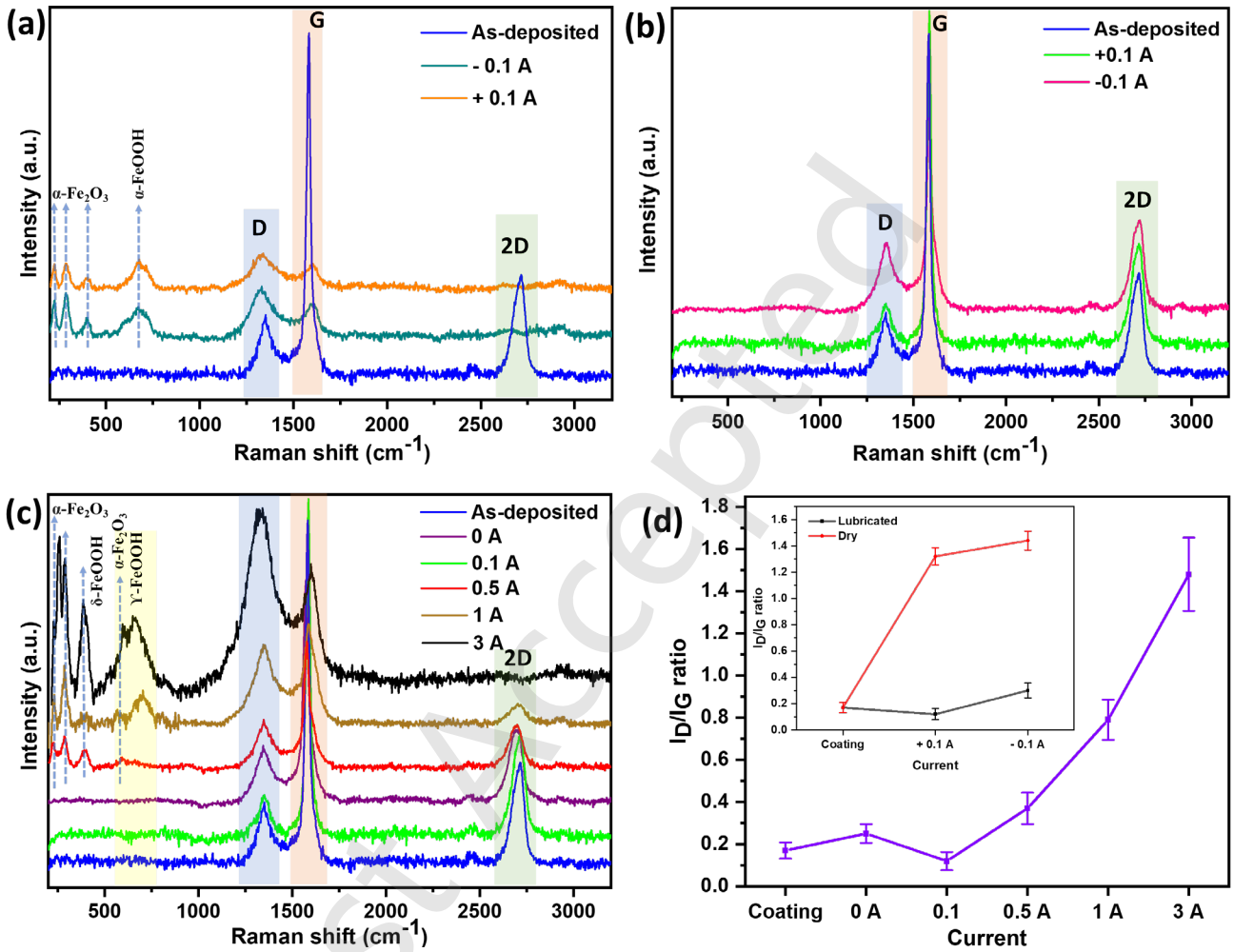


Fig. 12. Raman analysis of the GNP coated disk wear track under (a) dry sliding conditions with +0.1 and −0.1 A currents, (b) lubricated sliding conditions with +0.1 and −0.1 A currents, (c) lubricated sliding conditions with different currents (0-3 A), (d) I_D/I_G ratio with different electrical current under lubricated and inset shows I_D/I_G ratio under dry and lubricated sliding conditions for comparison.

Raman spectroscopy provides direct insights into the structural evolution of graphene nanoplatelets within the wear track and clarifies how electrical current and lubrication influence the tribofilm stability (Fig. 12). Raman analysis of the wear tracks under dry sliding with an applied current of ±0.1 A indicated substantial degradation and depletion of graphene within the contact region, consistent with the observed increase and instability of the CoF (Fig. 12a). Under dry sliding conditions, the

Just Accepted

characteristic G-band appears at ~1600 cm^{-1}, while the defect-related D-band appears at ~1339 cm^{-1} for both +0.1 A and −0.1 A (see Fig. 12a). The 2D-band was absent in both conditions, and the I_D/I_G ratio (~1.71 for +0.1 A and ~1.44 for −0.1 A) was significantly higher than for the as-deposited GNP coating (~0.17) (see inset of Fig. 12d). These results clearly suggest a loss of ordered sp^2 carbon structure and the transformation of graphene into a highly disordered, defect-rich graphitic phase during the sliding [59]. In addition, multiple peaks below 740 cm^{-1} correspond to iron oxides and hydroxides, confirming the exposure and oxidative damage of the steel substrate due to tribofilm failure [51,60]. These results suggest that electrical stimulation under dry sliding promotes rapid graphene degradation, likely driven by localized Joule heating, tribochemical oxidation, and interfacial delamination, ultimately leading to coating failure and unstable frictional behaviour [38,59].

Fig. 12c shows the Raman spectrum under aqueous glycerol lubrication with different electrical currents. For the 0 A sliding condition, the I_D/I_G ratio increased to ~0.25 compared with that of the as-deposited GNP coating (see Fig. 12d). The D-band located at ~1344.8 cm^{-1}, while the G-band remained sharp at ~1573.8 cm^{-1} with a well-defined 2D-band at 2690 cm^{-1} was observed. Moreover, the increase in the running-in time (~ 542 s, see Fig. 4) to achieve superlubricity could also be attributed to the introduction of additional defects in the graphene lattice due to the formation of C–H and C–OH bonds during sliding in the aqueous lubricant environment [61]. This reflects the formation of a mechanically stable graphene tribofilm, consistent with friction and wear results as shown in Fig. 4, Fig. 10 and Fig. 11.

When a positive current of +0.1 A was applied during lubricated sliding, the I_D/I_G ratio decreased to ~0.13 (close to that of the as-deposited GNP coating, see Fig. 12d), with a D-band around ~1352 cm^{-1} and a narrowed, well-defined G-band and prominent 2D-band at ~1589 and ~2725 cm^{-1}, respectively (see Fig. 12b). This indicates improved ordering of the graphene structure during sliding. The combination of shear, electrical double-layer effects, and mild Joule heating likely promotes the re-alignment of graphene platelets and partial recovery of structural order [23,62,63]. In contrast, when

Just Accepted

negative current (−0.1 A) was applied, the I_D/I_G ratio increased to ~0.30 (see inset of Fig. 12d) compared to 0 A, indicating the slower kinetics of the structural realignment and tribolayer formation under reverse polarity. The comparatively low peak intensity suggests that a fully developed adsorption film may not have formed [23], resulting in delayed superlubricity (i.e., after ~ 698 s) and higher wear compared to the +0.1 A sliding condition.

At higher applied currents (i.e., 0.5 A, 1 A, and 3 A) under lubricated sliding, Raman spectra reveal a systematic increase in structural disorder as evidenced by the increasing I_D/I_G ratio, together with the clear evidence of substrate involvement. The I_D/I_G ratios of 0.37, 0.79, and 1.47 were observed with 0.5 A, 1 A, and 3 A, respectively (see Fig. 12d), with a decreasing trend in G-band intensity. Thus, the D-band intensity increased and the 2D-band became very weak or completely disappeared with increasing current (see Fig. 12c). The higher I_D/I_G ratio, along with the presence of iron-oxide-related peaks as shown in Fig. 12c (typically around 225, ~290, ~410, ~560-593, 680, and ~704 cm^{-1}) [51,60], provide clear evidence of increasing structural disorder and tribofilm degradation. These Raman features correlate well with the observed friction fluctuations and increased wear volume, indicating that excessive current destabilizes the tribolayer through electrochemical overactivation and localized thermal effects. This clearly suggests a loss of ordered sp^2 carbon structure and the transformation of graphene into a highly disordered, defect-rich graphitic phase during sliding [59].

Overall, the Raman analysis establishes a clear structure-property relationship i.e., low I_D/I_G ratio with significant G-band and a well preserved 2D-band correspond to an ordered and structurally stabilized graphene tribofilm and super-lubricious sliding under low current with lubricant, whereas a higher D-band intensity resulting in high I_D/I_G ratio, and the presence of iron oxide peaks indicate tribofilm degradation, substrate exposure, and increased wear under dry and lubricated conditions at the highest current of 3 A. The +0.1 A lubricated condition provides an optimal balance between shear-induced graphene rearrangement and electrical stimulation, facilitating tribofilm stabilization, whereas higher currents disrupt the interfacial layer and promote accelerated tribological damage.

Just Accepted

3.5 XPS analysis of the worn surfaces

XPS analysis were used to investigate the tribochemical evolution of the worn surfaces formed under different electrified sliding conditions. Based on the friction and wear trends, only the surfaces lubricated under 0 A, +0.1 A, and 3 A were analysed and presented in Fig. 13. SXI imaging was used to ensure that spectra were collected within the wear-scars, with an analysis spot size of 50 µm. The XPS survey spectra (Fig. 13a) reveal the presence of C, O, and Fe. A high surface concentration of C suggests the formation of carbon-rich tribofilm with iron-based species (likely transferred from the steel counterpart). In addition, surface atomic concentrations of these elements were calculated using HR C 1s, O 1s, and Fe $2p_{3/2}$, as presented in Fig. 13b. The spectra reveal a lower Fe concentration on the surface lubricated under +0.1 A than under 0 A and 3 A, whereas the highest Fe content was observed under 3 A (see Fig. 13b). Notably, under +0.1 A (Fig. 13b), the surface concentrations of carbon and oxygen were 56.99 at. %, and 36.01 at. %, respectively, yielding a C/O ratio of 1.58. This ratio was higher than those measure at 0 A (1.35) and 3 A (0.90), indicating a more carbon-rich surface composition under +0.1 A. This further indicates that a graphene structure with limited surface oxidation covers the wear track, which can be favourable for maintaining structural integrity and load-bearing capability under sliding conditions. This trend agrees with the loss of superlubricity (Fig. 4c) and the increase in wear rate (Figs. 10-11), confirming increased metal exposure and material transfer under sliding at 3 A. Notably, the highest surface atomic concentration of carbon was detected at +0.1 A, suggesting enhanced retention and stability of graphene on the surface, which is consistent with the early superlubricity state within ~ 145 s (Fig. 4c–d) with very low wear rate (see Figs. 10-11).

The HR C 1s spectra were deconvoluted into five components corresponding to C–Fe (282.7 eV), C–C/C=C (284.5 eV), C–O (285.6 eV), C=O (287.0 eV), and O–C=O (288.2 eV). At 0 A (Fig. 13c-i), the surface contribution of C–C/C=C (i.e., 52.46%) slightly decreased compared to the as-deposited

Just Accepted

GNP coating (54.08%), while the C–O component increased to 30.38%, indicating a 32.4% increase compared to the C 1s obtained on the coating (Fig. 3e). This increase is likely due to additional hydroxylated species attached to the surface under aqueous lubricated conditions. Importantly, the C=O contribution decreased by 67.7 %, while the O–C=O contribution increased by 21.4 % compared to the GNP coating. As the C=O bonds originate from graphene oxide nanoflakes [64], their presence indicates that the graphene flakes remain intact within the wear track, resulting in superlubricity after 542 s (see Fig. 3c–d). These results are consistent with the Raman findings, showing minimal change in the I_D/I_G ratio (see Fig. 12d). In contrast, the surface lubricated under +0.1 A (Fig. 13d-i) shows a C–C/C=C contribution of 52.52%, suggesting that the graphitic nature of the coating is retained despite the influence of the sliding and the applied electrical current. Interestingly, the presence of the C–Fe peak becomes more pronounced (i.e., 4.12%), implying strong interfacial bonding between graphene and the steel substrate. This observation suggests that graphene remains firmly attached to the substrate and retains its graphitic nature, which agrees with the lowest I_D/I_G ratio obtained from the Raman spectroscopy (see Fig. 12d). The preservation of the sp^2 bonding under this condition is considered a key factor responsible for the observed early stable superlubricity (i.e., ~145 s, see Fig. 4c-d).

Under 3 A sliding conditions (Fig. 13e-i), the C 1s peak becomes broadened, reflecting the deformation and chemical disorder within the tribofilm [65–67]. This broadening indicates severe deformation of the tribofilm, caused by the extreme sliding conditions, accompanied by intense shearing and exfoliation of the graphene layers. Additionally, a pronounced reduction in the C–C/C=C contribution was observed (see Fig. 13e-i) in the C 1s spectrum, suggesting disruption of the sp^2 lattice. Such friction-induced damage to the graphene structure is consistent with Raman results showing increased disorder with high I_D/I_G ratios, indicating loss of graphitic integrity. The relatively high O–C=O contribution observed under all conditions is attributed to the tribochemical reactions between the glycerol (or its degradation products) and the oxidized steel surface [68,69].

Just Accepted

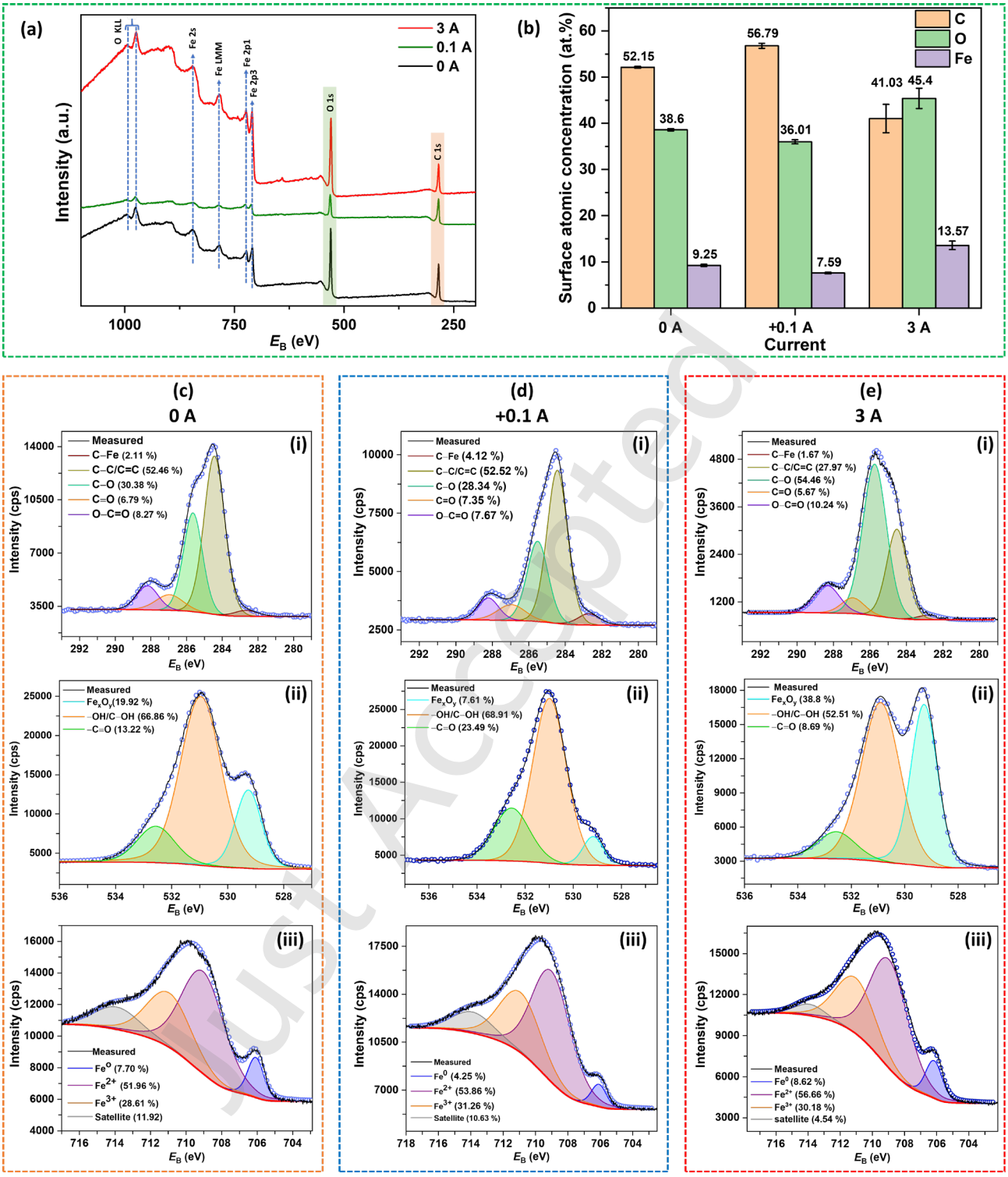


Fig. 13. XPS analysis conducted inside the wear tracks and the diameter of the analysis spot was 50 µm: (a) survey spectra, and (b) surface atomic concentration attained under electrical current of 0 A, +0.1 A and 3 A. HR XPS spectra for electrical current of (c) 0 A, (d) +0.1 A, and (e) 3 A: (i) C 1s, (ii) O 1s, and (iii) Fe $2p_{3/2}$.

The high-resolution O 1s spectrum (Fig. 13c-ii, Fig. 13d-ii, and Fig. 13e-ii) shows a peak at 529.3 eV corresponding to iron oxide (Fe_xO_y), while the second component 531.0 eV corresponds to interfacial

Just Accepted

or hydroxyl oxygen, including C–OH [18,51,68]. The higher surface contribution of this component correlates with the increase of the C–O contribution observed in the corresponding C 1s spectra, while the final component at E_B of 532.6 corresponds to C=O. These results suggest the formation of a hydrated, oxygen-rich surface layer of organic species /iron oxyhydroxides at the sliding interface [18]. Moreover, the HR O 1s spectra show that the relative surface contribution of the Fe_xO_y was minimal at +0.1 A (7.6%), while in the case of 0 A it was higher (19.9%). Notably, in the case of 3 A, the Fe_xO_y contribution was maximum (38.8%). These results are consistent with the friction and wear trends (see Fig. 4, Fig. 10, and Fig. 11).

Additionally, the Fe $2p_{3/2}$ spectra (Fig. 13c-iii, Fig. 13d-iii, and Fig. 13e-iii) show that under 3 A sliding, the metallic Fe signal becomes more pronounced, suggesting direct exposure of the steel substrate and increased material transfer from the steel ball. In contrast, under 0 A and +0.1 A, the Fe was mainly present in an oxidised state, suggesting that the graphene coating remains largely intact and continues to protect the steel surface. The oxidised Fe particles detected under these conditions (i.e, 0 and +0.1 A) are most likely transferred debris from the steel ball rather than the products of coating failure. Overall, the XPS results confirm that lubrication under +0.1 A promotes a stable, carbon-rich tribofilm with a preserved graphitic structure, and this behaviour is corroborated by the Raman results (Fig. 12), directly supporting the observed early superlubricity state (Fig. 4c) and negligible wear (Figs. 10-11) under +0.1 A sliding conditions.

4. Discussion

The present study demonstrates that the tribological performance of electrophoretically deposited GNP coatings on steel surface under aqueous glycerol lubrication is governed by the electrically regulated evolution of the graphene-derived tribofilm. Among all the investigated conditions, a mild positive current (+0.1 A) produced the most favourable tribological response by significantly reducing the running-in period from approximately 542 s to 145 s while maintaining a stable CoF of ~0.007 (Fig. 4). This improvement was accompanied by the lowest wear volume of the steel counterface and the

Just Accepted

lowest specific wear rate of the GNP coated disk, together with the highest final contact pressure (Fig. 7b), indicating the formation of a mechanically robust and chemically stable tribofilm. In contrast, increasing the applied current resulted in increasing instability of the sliding interface, accompanied by higher frictional fluctuations, increased wear, and the eventual loss of superlubricity at 3 A. These findings demonstrate that electrical stimulation does not simply reduce friction. It rather regulates the balance between tribofilm formation and tribofilm degradation, thereby defining a narrow electro-lubrication window for stable superlubricity.

The aqueous glycerol lubricant promotes tribofilm stability by transporting detached graphene fragments into the sliding interface and stabilising oxygen-containing defect sites through hydrogen-bonding interaction, thereby facilitating continuous tribofilm replenishment [40,58]. The improved tribological response under +0.1 A is supported by the complementary Raman and XPS analyses. Raman analysis (Fig. 12) demonstrates partial preservation of the graphitic structure, while XPS analysis (Fig. 13) shows the highest C/O ratio and lowest Fe surface concentration among the tested conditions. These results demonstrate that the sliding interface remains carbon-rich with limited oxidation compared to 0 A and 3 A, consistent with a stable graphene-rich tribofilm that promotes low-shear sliding and protects the underlying steel surface [62]. The preservation of the graphitic structure together with the reduced Fe exposure is consistent with the accelerated establishment of superlubricity and reduced wear observed under this condition [38,70].

However, increasing the applied current beyond +0.1 A destabilised the graphene-rich tribofilm, leading to a gradual deterioration in tribological performance. Although transient superlubricity was still achieved at 0.5 A and 1 A, but for a shorter period, accompanied by pronounced friction fluctuation towards the end of the tests (Fig.4c) which results in higher wear (Fig. 10-11). This degradation may attributed to excessive electrochemical oxidation and localized thermal effects that overwhelm the graphene defect-healing and tribofilm self-repair mechanisms, leading to severe wear in the absence of effective passivation [71]. Consistent with this interpretation, Raman spectroscopy revealed a

Just Accepted

continuous increase in the I_D/I_G ratio together with the weakening of the characteristic 2D band and the appearance of iron-oxide-related peaks (Fig. 12c), indicating increasing structural disorder and oxidation. This interpretation is further supported by the XPS analysis (Fig. 13) and it revealed a reduction in graphitic C–C/C=C bonding, along with an increase in oxygen-containing species and a stronger metallic Fe contribution, which resulted in higher friction and wear.

4.1 Proposed lubrication mechanism of electrically regulated superlubricity

The proposed lubrication mechanism shown in Fig. 14 is derived from the combined friction, wear and surface analysis results. Under aqueous glycerol lubricated sliding (0 A), stable superlubricity state was achieved after a relatively long running-in time of ~542 s (see Fig. 4e). The corresponding optical image (7a), wear profile (Fig. 8a), wear volume and specific wear rate (Figs. 10c and 11c), together with Raman and XPS analyses (Figs. 12 and 13) demonstrate that sliding promotes the gradual development of a graphene-rich tribofilm. During the running-in stage, partial delamination of the electrophoretically deposited coating release detached GNP in to the aqueous glycerol, where detached particles act as in-situ solid lubricant particles (Fig. 14a). Under repeated shear, these graphene sheets continuously align parallel to the sliding direction and form a dynamically replenished graphene-rich tribofilm, while simultaneously filling surface asperities and microcracks. The lamellar graphene structure facilitates easy interlayer sliding, thereby suppressing direct metal-to-metal contact and reduces interfacial shear resistance, while glycerol-water molecules stabilise the defected graphene through hydrogen bonding (see Fig. 14a) [51,54,72]. Simultaneously, tribochemical reactions on the steel surface promote the formation of hydroxyl-terminated Fe species (see Fig. 13c(ii-iii)). The internal chemistry is further influenced by shear-induced glycerol degradation, which generates acidic by-products, while water dissociation supplies H and OH species capable of reacting with exposed dangling bonds on the steel surface [50,51,54,68]. These reactions continuously produce a hydroxyl-rich and chemically stabilised interface by passivating reactive surface sites, as evidenced by the higher

Just Accepted

surface contribution from the interfacial or hydroxyl oxygen (see Fig. 13c-ii), thereby reducing interfacial interactions and facilitating the transition to superlubricity regime (see Fig. 4d).

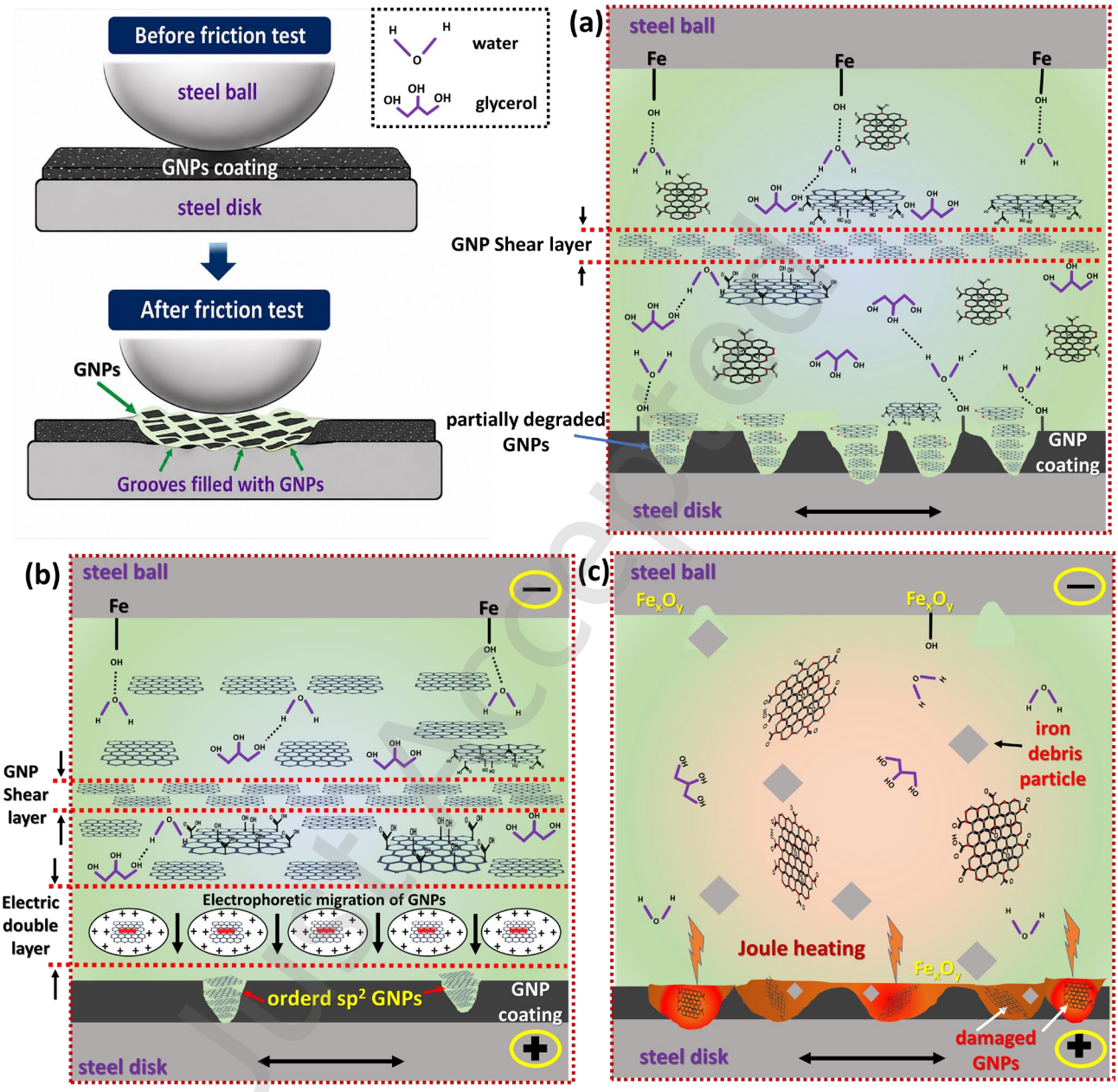


Fig. 14. Schematic of the proposed synergetic lubrication mechanisms under positive current polarity during sliding: (a) 0 A, illustrating the shear-induced alignment of GNP and limited interfacial passivation gradually lead to tribofilm formation; (b) +0.1 A, showing electrophoretic migration of graphene nanoplatelets, electrical double-layer formation, and current-assisted reordering of sp^2 carbon domains promote rapid tribofilm replenishment, groove filling, and a stable low-shear interface resulting in early superlubricity; and (c) 3 A, where excessive Joule heating with intensified electrochemical

reactions disrupt the graphene tribofilm, induce steel-surface oxidation (Fe_xO_y formation), generate iron related debris, and trigger a transition from a self-healing regime to tribofilm failure leading to coating failure.

Applying a mild positive current (+0.1 A) with the same polarity used during electrophoretic deposition fundamentally alters the evolution of the graphene-derived tribofilm (Fig. 14b). Under the applied electric field, protruding graphene nanoplatelets detached during the running-in stage migrate towards the disk surface, leading to the formation of an adsorbed graphene film. During the sliding, repeated interaction with the steel ball induces shear-assisted reorientation of the graphene layers, aligning them parallel to the sliding direction, which is favourable for low shear and protective tribofilm formation [23]. Simultaneously, the applied current can regulates the surface chemistry by maintaining a carbon-rich interface, thereby producing a smoother sliding interface with reduced interlayer shear between graphene nanosheets [70]. This behaviour is reflected in the significantly shorter running-in time (~145 s, Fig. 4d), and the lowest counterface wear, accompanied by the shallowest wear profile and smallest wear-scar (Figs. 4, 7b and 8b), and consequently the lowest wear rate (Fig. 11c), demonstrating that the graphene-rich tribofilm effectively protects the sliding interface. The structural and chemical analyses further support this mechanism. XPS analysis (Fig. 13b) demonstrated the highest C/O ratio with the lowest Fe surface concentration, confirming the formation of a carbon-rich and chemically stable interface that favours smoother sliding and reduced interlayer shear between graphene nanosheets [73–75]. Consistently, Raman spectroscopy (Fig. 12b) revealed no pronounced iron-oxide-related features, indicating limited interfacial oxidation under this condition. Furthermore, the enhanced tribological performance is further attributed to electrically regulated interfacial processes. The formation of an EDL at the graphene-electrolyte-steel interface is proposed to reduce interfacial shear stress while simultaneously promoting the electrophoretic migration of negatively charged graphene nanoplatelets toward the wear track [73–75]. Continuous replenishment of graphene at the sliding interface rapidly covers defect generated during sliding, thereby enhancing self-healing capability of the tribofilm. In addition, electron transport through the coating and across the sliding junction is likely to generate a localised electrical field accompanied by mild Joule heating

Just Accepted

at the asperity contact. These localized electrical and thermal effects may promote current-induced annealing, facilitating partial restoration of the sp^2 carbon domains and improving the self-healing of defected graphene within the tribofilm [73–78]. Furthermore, hydrogen bonding between glycerol/water molecules and oxygenated defect sites at graphene edges enhances the dispersion and flow of graphene fragments into the sliding interface while partially passivating dangling bonds [18,32]. This hydrated passivation further stabilises the tribofilm and suppresses oxidative and adhesive wear, consistent with the Raman (Fig. 12) and XPS (Fig. 13) analysis.

Under higher current, the electrically stimulated graphene-lubrication system shifts from a self-healing regime to a failure-dominated state, resulting in the loss of the superlubricity and severe wear (Fig. 14c). This transition is directly evidenced by the larger wear-scar diameter (Fig. 7f) and higher wear depth profile (Fig. 9c), and consequently higher wear volume and wear rate (Figs. 10c and 11c), demonstrating that graphene tribofilm loses its load-bearing and protective capability. Consistent with these tribological observations, Raman spectroscopy (Fig. 12) revealed a substantial increase in the I_D/I_G ratio together with pronounced iron oxide-related peaks, while XPS analysis (Fig. 13) revealed a reduction in graphitic C–C/C=C bonding accompanied by increased oxygen-containing species and metallic Fe contribution. Collectively, these analyses confirm severe structural degradation of the graphene tribofilm together with continuous exposure and oxidation of the steel substrate. This deterioration is attributed to the combined effects of current-induced Joule heating, frictional heating, and electrochemically driven oxidation at the sliding interface [71,79]. These processes are proposed to accelerate defect accumulation within the graphene structure, weaken the sp^2 bonded carbon network, and promote interfacial delamination, thereby reducing the mechanical integrity of the tribofilm. As the protective graphene layer gradually deteriorates, direct asperity interaction between the opposing steel surfaces becomes increasingly dominant, promoting a transition from predominantly adhesive to abrasive wear [46,79]. The localised frictional heating further promotes interfacial oxidation and facilitates crack initiation and propagation within the carbon layer [18], which

Just Accepted

is consistent with the iron-oxide-related Raman features (Fig. 12c) together with increased oxidized Fe and O contributions as evidenced in the XPS analysis (Fig. 13b & e). Consequently, the tribofilm degradation rate exceeds its replenishment rate, leading to unstable friction, extensive material removal, and the eventual loss of superlubricity (see Figs. 10-11). Therefore, stable superlubricity is maintained only when graphene tribofilm replenishment exceeds tribofilm degradation, whereas excessive electrical loading reverses this balance, resulting in tribofilm failure and severe wear.

In summary, from an engineering perspective, the proposed lubrication strategy offers an attractive alternative to conventional graphene nano-additive lubrication. Instead of relying on long-term dispersion stability of graphene within the lubricant, the electrophoretically deposited coating serves as a continuous graphene reservoir that supplies fresh material to the sliding interface throughout function. Combined with aqueous glycerol lubrication and controlled electrical stimulation, this approach enables adaptive tribofilm renewal while maintaining low friction and wear under boundary-lubricated conditions. Such electrically regulated lubrication strategy is particularly relevant to engineering systems involving reciprocating sliding, variable contact loads and electrical stimulation. More importantly, the present results establish that electrical current can be used as an active parameter to regulate graphene tribofilm evolution, thereby controlling both the onset and stability of superlubricity. This concept provides a practical framework for the rational design of adaptive graphene-based lubrication systems for future electrified tribological applications.

Just Accepted

5. Conclusion

This study presents an effective strategy for achieving rapid superlubricity on steel surfaces by depositing a GNP coating using the electrophoretic deposition technique under aqueous glycerol lubrication.

i. A low current (+0.1 A) significantly shortens the running-in period (~145 s) and promotes early superlubricity. The wear volume of the steel counterface ball was decreased by ~33% compared

to non-electrified sliding (0 A), reflecting enhanced tribofilm stabilisation and defect-induced structural reordering within the graphene layer.

ii. In contrast, at higher current (3 A), the CoF and ball wear volume increased to ~0.065 and ~1.01×10^{-4} mm^3, respectively owing to excessive Joule heating and interfacial oxidation that destabilised the protective graphene tribofilm.

iii. These findings reveal a narrow electro-lubrication window in which electrical stimulation promotes nanosheet alignment, interfacial regulation, and active tribofilm replenishment.

Overall, these findings highlight the strong potential of graphene-based coatings for electrically regulated ultra-low-friction interfaces and provide a mechanistic insight for designing energy-efficient, ultra-low-friction tribological interfaces.

Not Accepted

Acknowledgement

The authors acknowledge the financial support of the Slovenian Research Agency ARIS under the Research Core Funding Programme No. P2-0231 and the project MSCA-COFUND-5100-237/2023-9.

References

[1] K. Holmberg, A. Erdemir, Influence of tribology on global energy consumption, costs and emissions, Friction 5 (2017) 263–284. https://doi.org/10.1007/s40544-017-0183-5.

[2] W. Ahmed Abdalglil Mustafa, F. Dassenoy, M. Sarno, A. Senatore, A review on potentials and challenges of nanolubricants as promising lubricants for electric vehicles, Lubrication Science 34 (2022) 1–29. https://doi.org/10.1002/ls.1568.

[3] H.P. Jost, J. Schofield, Energy Saving through Tribology: A Techno-Economic Study, Proceedings of the Institution of Mechanical Engineers 195 (1981) 151–173. https://doi.org/10.1243/PIME_PROC_1981_195_016_02.

[4] K. Holmberg, A. Erdemir, The impact of tribology on energy use and CO2 emission globally and in combustion engine and electric cars, Tribology International 135 (2019) 389–396. https://doi.org/10.1016/j.triboint.2019.03.024.

[5] A.G. Tuero, C. Sanjurjo, N. Rivera, J.L. Viesca, R. González, A.H. Battez, Electrical conductivity and tribological behavior of an automatic transmission fluid additised with a phosphonium-based ionic liquid, Journal of Molecular Liquids 367 (2022) 120581. https://doi.org/10.1016/j.molliq.2022.120581.

[6] F. He, G. Xie, J. Luo, Electrical bearing failures in electric vehicles, Friction 8 (2020) 4–28. https://doi.org/10.1007/s40544-019-0356-5.

[7] K. Esmaeili, L. Wang, T.J. Harvey, N.M. White, W. Holweger, Electrical Discharges in Oil-Lubricated Rolling Contacts and Their Detection Using Electrostatic Sensing Technique, Sensors 22 (2022) 392. https://doi.org/10.3390/s22010392.
[8] P.L. Alger, H.W. Samson, Shaft Currents in Electric Machines, Trans. Am. Inst. Electr. Eng. XLIII (1924) 235–245. https://doi.org/10.1109/T-AIEE.1924.5060981.
[9] G.K. Singh, S. Ahmed Saleh Al Kazzaz, Induction machine drive condition monitoring and diagnostic research—a survey, Electric Power Systems Research 64 (2003) 145–158. https://doi.org/10.1016/S0378-7796(02)00172-4.
[10] R. Mukherjee, A. Patra, S. Banerjee, Impact of a Frequency Modulated Pulsewidth Modulation (PWM) Switching Converter on the Input Power System Quality, IEEE Trans. Power Electron. 25 (2010) 1450–1459. https://doi.org/10.1109/TPEL.2009.2037421.
[11] S. Nandi, H.A. Toliyat, X. Li, Condition Monitoring and Fault Diagnosis of Electrical Motors—A Review, IEEE Trans. On Energy Conversion 20 (2005) 719–729. https://doi.org/10.1109/TEC.2005.847955.
[12] K.B. Tawfiq, M. Güleç, P. Sergeant, Bearing Current and Shaft Voltage in Electrical Machines: A Comprehensive Research Review, Machines 11 (2023) 550. https://doi.org/10.3390/machines11050550.
[13] P. Zhang, Y. Du, T.G. Habetler, B. Lu, A Survey of Condition Monitoring and Protection Methods for Medium-Voltage Induction Motors, IEEE Trans. on Ind. Applicat. 47 (2011) 34–46. https://doi.org/10.1109/TIA.2010.2090839.
[14] Y. Chen, S. Jha, A. Raut, W. Zhang, H. Liang, Performance Characteristics of Lubricants in Electric and Hybrid Vehicles: A Review of Current and Future Needs, Front. Mech. Eng. 6 (2020) 571464. https://doi.org/10.3389/fmech.2020.571464.
[15] W. Ost, P. De Baets, Failure analysis of the deep groove ball bearings of an electric motor, Engineering Failure Analysis 12 (2005) 772–783. https://doi.org/10.1016/j.engfailanal.2004.12.003.
[16] H.C. Walther, R.A. Holub, Lubrication of electric motors as defined by IEEE standard 841-2009, shortcomings and potential improvement opportunities, in: 2014 IEEE Petroleum and Chemical Industry Technical Conference (PCIC), IEEE, San Francisco, CA, USA, 2014: pp. 91–98. https://doi.org/10.1109/PCICon.2014.6961872.
[17] P. Boškoski, J. Petrovčič, B. Musizza, Đ. Juričić, Detection of lubrication starved bearings in electrical motors by means of vibration analysis, Tribology International 43 (2010) 1683–1692. https://doi.org/10.1016/j.triboint.2010.03.018.
[18] P. Kumar, I. Nadeem, A. Naseer, T.B. Yaqub, A. Morina, M. Kalin, Superlubricity of diamond-like carbon coating lubricated with aqueous glycerol under electrified sliding conditions, Tribology International 215 (2026) 111415. https://doi.org/10.1016/j.triboint.2025.111415.
[19] D. Berman, L.I. Farfan-Cabrera, A. Rosenkranz, A. Erdemir, Advancing the frontiers of EV tribology with 2D materials – A critical perspective, Materials Science and Engineering: R: Reports 161 (2024) 100855. https://doi.org/10.1016/j.mser.2024.100855.
[20] D. Berman, L.I. Farfan-Cabrera, A. Rosenkranz, A. Erdemir, 2D materials for durable and sustainable electric vehicles, Nat Rev Mater 9 (2024) 527–529. https://doi.org/10.1038/s41578-024-00680-3.
[21] N.R. Glavin, R. Rao, V. Varshney, E. Bianco, A. Apte, A. Roy, E. Ringe, P.M. Ajayan, Emerging Applications of Elemental 2D Materials, Advanced Materials 32 (2020) 1904302. https://doi.org/10.1002/adma.201904302.
[22] M. Marian, D. Berman, A. Rota, R.L. Jackson, A. Rosenkranz, Layered 2D Nanomaterials to Tailor Friction and Wear in Machine Elements—A Review, Adv Materials Inter 9 (2022) 2101622. https://doi.org/10.1002/admi.202101622.
[23] X. Ge, L. Zhang, Q. Shi, Y. Xing, Y. Liu, Z. Cao, W. Wang, Facilitating macroscopic superlubricity through electric stimulation with graphene oxide nanosheet additives for steel

Just Accepted

surface lubrication, Applied Surface Science 661 (2024) 160039. https://doi.org/10.1016/j.apsusc.2024.160039.
[24] S. Batool, M. Idrees, S. Han, V.A.L. Roy, Y. Zhou, Electrical Contacts With 2D Materials: Current Developments and Future Prospects, Small 19 (2023) 2206550. https://doi.org/10.1002/smll.202206550.
[25] X. Hu, J. Lee, D. Berman, A. Martini, Substrate effect on electrical conductance at a nanoasperity-graphene contact, Carbon 137 (2018) 118–124. https://doi.org/10.1016/j.carbon.2018.05.028.
[26] I. Nadeem, T.B. Yaqub, M. Finšgar, P. Kumar, G. Dražić, M. Kalin, Durable and robust macroscale superlubricity on engineering steel enabled by nitrogen-doped graphene nanosheets, Carbon (2026) 122200. https://doi.org/10.1016/j.carbon.2026.122200.
[27] X. Ge, Z. Chai, Q. Shi, Y. Liu, W. Wang, Graphene superlubricity: A review, Friction 11 (2023) 1953–1973. https://doi.org/10.1007/s40544-022-0681-y.
[28] Y. Liu, J. Li, X. Ge, S. Yi, H. Wang, Y. Liu, J. Luo, Macroscale Superlubricity Achieved on the Hydrophobic Graphene Coating with Glycerol, ACS Appl. Mater. Interfaces 12 (2020) 18859–18869. https://doi.org/10.1021/acsami.0c01515.
[29] Y. Liu, L. Chen, L. Liu, P. Shi, J. Sun, Y. Wang, L. Qian, Macroscopic ultra-low friction and wear enabled by carboxylated graphene with glycerol, Applied Surface Science 638 (2023) 158028. https://doi.org/10.1016/j.apsusc.2023.158028.
[30] Q. Ma, T. He, A.M. Khan, Q. Wang, Y.-W. Chung, Achieving macroscale liquid superlubricity using glycerol aqueous solutions, Tribology International 160 (2021) 107006. https://doi.org/10.1016/j.triboint.2021.107006.
[31] Z. Chen, Y. Liu, J. Luo, Superlubricity of nanodiamonds glycerol colloidal solution between steel surfaces, Colloids and Surfaces A: Physicochemical and Engineering Aspects 489 (2016) 400–406. https://doi.org/10.1016/j.colsurfa.2015.10.062.
[32] I. Nadeem, M. Malok, J. Kovač, T. Bin Yaqub, A. Cavaleiro, M. Kalin, Superior macro-scale tribological performance of steel contacts based on graphene quantum dots in aqueous glycerol, Tribology International 181 (2023) 108328. https://doi.org/10.1016/j.triboint.2023.108328.
[33] D. Berman, A. Erdemir, A.V. Sumant, Graphene as a protective coating and superior lubricant for electrical contacts, Applied Physics Letters 105 (2014) 231907. https://doi.org/10.1063/1.4903933.
[34] F. Mao, U. Wiklund, A.M. Andersson, U. Jansson, Graphene as a lubricant on Ag for electrical contact applications, J Mater Sci 50 (2015) 6518–6525. https://doi.org/10.1007/s10853-015-9212-9.
[35] H. Lang, Y. Xu, P. Zhu, Y. Peng, K. Zou, K. Yu, Y. Huang, Superior lubrication and electrical stability of graphene as highly effective solid lubricant at sliding electrical contact interface, Carbon 183 (2021) 53–61. https://doi.org/10.1016/j.carbon.2021.07.016.
[36] D.W. Wang, F.Q. Li, X. Chen, Z.Y. Xiang, F. Zhao, Probing the effect of the electric current on the tribological performances of the electrical contact surfaces with graphene coating, Tribology International 178 (2023) 108121. https://doi.org/10.1016/j.triboint.2022.108121.
[37] L. Wang, Q. Tang, T. Liang, C. Liu, D. Sun, S. Wang, J. Li, S. Zhang, Y. Meng, Y. Huang, Lubrication performance of graphene in the sliding electrical contact interface, Friction 12 (2024) 2760–2773. https://doi.org/10.1007/s40544-024-0910-7.
[38] Q. Hu, Q. Shi, X. Ge, Y. Liu, Z. Zhao, W. Wang, T. Zhou, Study of graphene-family nanomaterials as grease additives for electro-regulated friction, Friction (2025). https://doi.org/10.26599/FRICT.2025.9441169.
[39] L. Besra, M. Liu, A review on fundamentals and applications of electrophoretic deposition (EPD), Progress in Materials Science 52 (2007) 1–61. https://doi.org/10.1016/j.pmatsci.2006.07.001.

Just Accepted

[40] A. Chavez-Valdez, M.S.P. Shaffer, A.R. Boccaccini, Applications of Graphene Electrophoretic Deposition. A Review, J. Phys. Chem. B 117 (2013) 1502–1515. https://doi.org/10.1021/jp3064917.
[41] G. Baiocco, E. Menna, D. Salvi, N. Ucciardello, Investigating tribological properties of electrophoretically deposited graphene nanoplatelets coatings on mild steel, Thin Solid Films 793 (2024) 140279. https://doi.org/10.1016/j.tsf.2024.140279.
[42] A.R. Boccaccini, J. Cho, J.A. Roether, B.J.C. Thomas, E. Jane Minay, M.S.P. Shaffer, Electrophoretic deposition of carbon nanotubes, Carbon 44 (2006) 3149–3160. https://doi.org/10.1016/j.carbon.2006.06.021.
[43] M. Diba, D.W.H. Fam, A.R. Boccaccini, M.S.P. Shaffer, Electrophoretic deposition of graphene-related materials: A review of the fundamentals, Progress in Materials Science 82 (2016) 83–117. https://doi.org/10.1016/j.pmatsci.2016.03.002.
[44] J. Wu, Understanding the Electric Double-Layer Structure, Capacitance, and Charging Dynamics, Chem. Rev. 122 (2022) 10821–10859. https://doi.org/10.1021/acs.chemrev.2c00097.
[45] J.A. Trejo González, M.P. Longinotti, H.R. Corti, The Viscosity of Glycerol−Water Mixtures Including the Supercooled Region, J. Chem. Eng. Data 56 (2011) 1397–1406. https://doi.org/10.1021/je101164q.
[46] P. Kumar, T.B. Yaqub, R. Kumar, I. Nadeem, A. Morina, M. Kalin, Electro-stimulated tribological behavior of DLC coatings under unlubricated sliding conditions, Tribology International 215 (2026) 111451. https://doi.org/10.1016/j.triboint.2025.111451.
[47] K. Sun, D. Diao, Current density effect on current-carrying friction of amorphous carbon film, Carbon 157 (2020) 113–119. https://doi.org/10.1016/j.carbon.2019.10.005.
[48] M.F. Wani, Mechanical and Tribological Properties of a Nano-Si_3N_4 /Nano-BN Composite, Int J Applied Ceramic Tech 7 (2010) 512–517. https://doi.org/10.1111/j.1744-7402.2009.02362.x.
[49] Handbook of X-Ray Photoelectron Spectroscopy A Reference Book of Standard Spectra for Identification and Interpretation of XPS Data, n.d.
[50] I. Nadeem, B. Ambrožič, G. Dražić, J. Kovač, A. Cavaleiro, M. Kalin, Super-low friction and wear in steel contacts enabled by tribo-induced structural degradation of graphene quantum dots, Materials & Design 244 (2024) 113111. https://doi.org/10.1016/j.matdes.2024.113111.
[51] I. Nadeem, M. Finšgar, G. Dražić, M. Malok, A. Morina, M. Kalin, Robust and durable superlubricity enabled by carboxylated graphene quantum dots in lubricated steel contacts, Carbon 226 (2024) 119226. https://doi.org/10.1016/j.carbon.2024.119226.
[52] D. Franzosi, J.C.F. De Queiroz, E. Tomanik, W. Christinelli, F.J. Profito, R.M. Souza, Exploring the potential of graphene nanoplatelets as a lubricant additive: Topography evolution and performance under boundary lubrication conditions, Tribology International 192 (2024) 109282. https://doi.org/10.1016/j.triboint.2024.109282.
[53] V. Georgakilas, M. Otyepka, A.B. Bourlinos, V. Chandra, N. Kim, K.C. Kemp, P. Hobza, R. Zboril, K.S. Kim, Functionalization of Graphene: Covalent and Non-Covalent Approaches, Derivatives and Applications, Chem. Rev. 112 (2012) 6156–6214. https://doi.org/10.1021/cr3000412.
[54] I. Nadeem, M. Finšgar, G. Dražić, B. Ambrožič, M. Malok, A. Cavaleiro, M. Kalin, Macroscale Superlubricity with a High Load-Carrying Capacity Enabled by Nitrogen-Doped Graphene Quantum Dots in Lubricated Silicon-Doped Amorphous Carbon Films, Small Structures 6 (2025) 2400671. https://doi.org/10.1002/sstr.202400671.
[55] X. Ge, J. Li, H. Wang, C. Zhang, Y. Liu, J. Luo, Macroscale superlubricity under extreme pressure enabled by the combination of graphene-oxide nanosheets with ionic liquid, Carbon 151 (2019) 76–83. https://doi.org/10.1016/j.carbon.2019.05.070.
[56] X. Ren, X. Yang, G. Xie, F. He, R. Wang, C. Zhang, D. Guo, J. Luo, Superlubricity under ultrahigh contact pressure enabled by partially oxidized black phosphorus nanosheets, Npj 2D Mater Appl 5 (2021) 44. https://doi.org/10.1038/s41699-021-00225-0.

Just Accepted

[57] S. Bhowmick, Z. Yang, A.T. Alpas, Tribochemical stability and friction mechanisms of graphene nanoplatelets in engine oil at elevated temperatures, Diamond and Related Materials 159 (2025) 112838. https://doi.org/10.1016/j.diamond.2025.112838.
[58] S. Singh, P. Verma, R.K. Gautam, R. Tyagi, Effect of counterface materials on friction and wear of graphene-coated steel under dry sliding contact, Materials Today: Proceedings 47 (2021) 6660–6663. https://doi.org/10.1016/j.matpr.2021.05.108.
[59] A.C. Ferrari, J. Robertson, Interpretation of Raman spectra of disordered and amorphous carbon, Phys. Rev. B 61 (2000) 14095–14107. https://doi.org/10.1103/PhysRevB.61.14095.
[60] K. Tripathi, G. Gyawali, S.W. Lee, Graphene Coating via Chemical Vapor Deposition for Improving Friction and Wear of Gray Cast Iron at Interfaces, ACS Appl. Mater. Interfaces 9 (2017) 32336–32351. https://doi.org/10.1021/acsami.7b07922.
[61] A.C. Ferrari, J.C. Meyer, V. Scardaci, C. Casiraghi, M. Lazzeri, F. Mauri, S. Piscanec, D. Jiang, K.S. Novoselov, S. Roth, A.K. Geim, Raman Spectrum of Graphene and Graphene Layers, Phys. Rev. Lett. 97 (2006) 187401. https://doi.org/10.1103/PhysRevLett.97.187401.
[62] M.B. Wakchaure, P.L. Menezes, Advances in the Tribological Performance of Graphene Oxide and Its Composites, Materials 18 (2025) 3587. https://doi.org/10.3390/ma18153587.
[63] J. Zhao, G. Chen, W. Zhang, P. Li, L. Wang, Q. Yue, H. Wang, R. Dong, X. Yan, J. Liu, High-Resolution Separation of Graphene Oxide by Capillary Electrophoresis, Anal. Chem. 83 (2011) 9100–9106. https://doi.org/10.1021/ac202136n.
[64] X. Ge, J. Li, R. Luo, C. Zhang, J. Luo, Macroscale Superlubricity Enabled by the Synergy Effect of Graphene-Oxide Nanoflakes and Ethanediol, ACS Appl. Mater. Interfaces 10 (2018) 40863–40870. https://doi.org/10.1021/acsami.8b14791.
[65] R. Blume, D. Rosenthal, J. Tessonnier, H. Li, A. Knop-Gericke, R. Schlögl, Characterizing Graphitic Carbon with X-ray Photoelectron Spectroscopy: A Step-by-Step Approach, ChemCatChem 7 (2015) 2871–2881. https://doi.org/10.1002/cctc.201500344.
[66] H. Estrade-Szwarckopf, XPS photoemission in carbonaceous materials: A "defect" peak beside the graphitic asymmetric peak, Carbon 42 (2004) 1713–1721. https://doi.org/10.1016/j.carbon.2004.03.005.
[67] R. Schlögl, H.P. Boehm, Influence of crystalline perfection and surface species on the X-ray photoelectron spectra of natural and synthetic graphites, Carbon 21 (1983) 345–358. https://doi.org/10.1016/0008-6223(83)90127-6.
[68] Y. Long, M.-I.D.B. Bouchet, T. Lubrecht, T. Onodera, J.M. Martin, Superlubricity of glycerol by self-sustained chemical polishing, Sci Rep 9 (2019) 6286. https://doi.org/10.1038/s41598-019-42730-9.
[69] Y. Long, M.-I.D. Barros Bouchet, A. Ristic, N. Dörr, J.M. Martin, Chapter 13 - Superlubricity of glycerol is enhanced in the presence of graphene or graphite, in: A. Erdemir, J.M. Martin, J. Luo (Eds.), Superlubricity (Second Edition), Elsevier, 2021: pp. 231–245. https://doi.org/10.1016/B978-0-444-64313-1.00013-2.
[70] J.A. Cao-Romero-Gallegos, L.I. Farfan-Cabrera, A. Erdemir, J.B. Pascual-Francisco, Lubricated sliding wear of gear material under electrification – A new approach to understanding of the influence of shaft currents in the wear of EV transmissions, Wear 523 (2023) 204782. https://doi.org/10.1016/j.wear.2023.204782.
[71] Q. Tang, Y. Huang, D. Sun, Q. Li, Effect of Humidity on the Wear Behavior of Graphene Under Current Carrying Conditions, Tribol Lett 73 (2025) 8. https://doi.org/10.1007/s11249-024-01946-1.
[72] S. Singh, X. Chen, C. Zhang, R. Tyagi, J. Luo, Investigation on the lubrication potential of graphene oxide aqueous dispersion for self-mated stainless steel tribo-pair, Vacuum 166 (2019) 307–315. https://doi.org/10.1016/j.vacuum.2019.05.015.
[73] Y. Zhang, W. Long, T. Li, L. Sun, M. Liu, Synergistic Enhancement Mechanism of Electric Double Layer Structure and Interfacial Tribochemical Reactions Regulated by pH in Water-

Just Accepted

Based Lubrication Systems, Langmuir 42 (2026) 1008–1019. https://doi.org/10.1021/acs.langmuir.5c05126.
[74] H.A. Spikes, Triboelectrochemistry: Influence of Applied Electrical Potentials on Friction and Wear of Lubricated Contacts, Tribol Lett 68 (2020) 90. https://doi.org/10.1007/s11249-020-01328-3.
[75] H. Tang, X. Chen, W. Deng, J. Luo, Comprehensive review: Advances and critical mechanisms in liquid superlubricity, Advances in Colloid and Interface Science 344 (2025) 103585. https://doi.org/10.1016/j.cis.2025.103585.
[76] J. Zhu, D. Shi, A possible self-healing mechanism in damaged graphene by heat treatment, Computational Materials Science 68 (2013) 391–395. https://doi.org/10.1016/j.commatsci.2012.10.041.
[77] J. Chen, T. Shi, T. Cai, T. Xu, L. Sun, X. Wu, D. Yu, Self healing of defected graphene, Applied Physics Letters 102 (2013) 103107. https://doi.org/10.1063/1.4795292.
[78] P.-C. Lin, R. Villarreal, H. Bana, Z. Zarkua, V. Hendriks, H.-C. Tsai, M. Auge, F. Junge, H. Hofsäss, E. Tosi, P. Lacovig, S. Lizzit, W. Zhao, G. Di Santo, L. Petaccia, S. De Feyter, S. De Gendt, S. Brems, L.M.C. Pereira, Thermal Annealing of Graphene Implanted with Mn at Ultralow Energies: From Disordered and Contaminated to Nearly Pristine Graphene, J. Phys. Chem. C 126 (2022) 10494–10505. https://doi.org/10.1021/acs.jpcc.2c00855.
[79] P. Huang, D. Guo, G. Xie, J. Li, Softened Mechanical Properties of Graphene Induced by Electric Field, Nano Lett. 17 (2017) 6280–6286. https://doi.org/10.1021/acs.nanolett.7b02965.

Authors biography



Parveen Kumar received his Ph.D. in Mechanical Engineering from the National Institute of Technology Srinagar, India, in 2018. He is currently working as a Mobility GT Postdoctoral Researcher at the Laboratory for Tribology and Interface Nanotechnology (TINT), University of Ljubljana, Slovenia. His research interests include tribology of advanced materials, DLC coatings, graphene-based lubrication, and electrified tribology, with a particular focus on friction and wear mechanisms, tribochemistry, and electrically induced superlubricity.

Just Accepted



Mitjan Kalin received his Ph.D. in Mechanical Engineering from the University of Ljubljana, Slovenia, in 1999. After postdoctoral research at the National Institute of Standards and Technology (NIST), USA, he joined the University of Ljubljana in 2000, where he is currently a Full Professor and Head of the Laboratory for Tribology and Interface Nanotechnology (TINT). His research interests include friction and wear of advanced materials, boundary lubrication and tribochemistry, DLC coatings, interfacial phenomena, superlubricity, and environmentally friendly lubrication technologies.

Just Accepted